Chapter 2
The Interaction of Radiation with Matter

Hans Bichsel and Heinrich Schindler

2.1 Introduction

The detection of charged particles is usually based on their electromagnetic interactions with the electrons and nuclei of a detector medium. Interaction with the Coulomb field of the nucleus leads to deflections of the particle trajectory (multiple scattering) and to radiative energy loss (bremsstrahlung). Since the latter, discussed in Sect. 2.4.1, is inversely proportional to the particle mass squared, it is most significant for electrons and positrons.

"Heavy" charged particles (in this context: particles with a mass M exceeding the electron mass m) passing through matter lose energy predominantly through collisions with electrons. Our theoretical understanding of this process, which has been summarised in a number of review articles [1–7] and textbooks [8–13], is based on the works of some of the most prominent physicists of the twentieth century, including Bohr [14, 15], Bethe [16, 17], Fermi [18, 19], and Landau [20].

After outlining the quantum-mechanical description of single collisions in terms of the double-differential cross section $\mathrm{d}^2\sigma/(\mathrm{d}E\mathrm{d}q)$, where E and q are the energy transfer and momentum transfer involved in the collision, Sect. 2.3 discusses algorithms for the quantitative evaluation of the single-differential cross section

The author Hans Bichsel is deceased at the time of publication.

H. Bichsel · H. Schindler (✉)
CERN, Geneva, Switzerland
e-mail: Heinrich.Schindler@cern.ch

C. W. Fabjan, H. Schopper (eds.), *Particle Physics Reference Library*,
https://doi.org/10.1007/978-3-030-35318-6_2

$\mathrm{d}\sigma/\mathrm{d}E$ and its moments. The integral cross section (zeroth moment), multiplied by the atomic density N, corresponds to the charged particle's inverse mean free path λ^{-1} or, in other words, the average number of collisions per unit track length,

$$\lambda^{-1} = M_0 = N \int_{E_{\min}}^{E_{\max}} \frac{\mathrm{d}\sigma}{\mathrm{d}E} \mathrm{d}E. \tag{2.1}$$

The stopping power $\mathrm{d}E/\mathrm{d}x$, i.e. the average energy loss per unit track length, is given by the first moment,

$$-\frac{\mathrm{d}E}{\mathrm{d}x} = M_1 = N \int_{E_{\min}}^{E_{\max}} E \frac{\mathrm{d}\sigma}{\mathrm{d}E} \mathrm{d}E. \tag{2.2}$$

The integration limits $E_{\min,\,\max}$ are determined by kinematics. Due to the stochastic nature of the interaction process, the number of collisions and the sum Δ of energy losses along a particle track are subject to fluctuations. Section 2.5 deals with methods for calculating the probability density distribution $f(\Delta, x)$ for different track lengths x. The energy transfer from the incident particle to the electrons of the medium typically results in excitation and ionisation of the target atoms. These observable effects are discussed in Sect. 2.6.

As a prologue to the discussion of charged-particle collisions, Sect. 2.2 briefly reviews the principal photon interaction mechanisms in the X-ray and gamma ray energy range.

Throughout this chapter, we attempt to write all expressions in a way independent of the system of units (cgs or SI), by using the fine structure constant $\alpha \sim 1/137$. Other physical constants used occasionally in this chapter include the Rydberg energy $\mathrm{Ry} = \alpha^2 mc^2/2 \sim 13.6\,\mathrm{eV}$, and the Bohr radius $a_0 = \hbar c/\left(\alpha mc^2\right) \sim 0.529\,\text{Å}$. Cross-sections are quoted in barn ($1\,\mathrm{b} = 10^{-24}\,\mathrm{cm}^2$).

2.2 Photon Interactions

Photons interact with matter via a range of mechanisms, which can be classified according to the type of target, and the effect of the interaction on the photon (absorption or scattering) [9, 21]. At energies beyond the ultraviolet range, the dominant processes are photoelectric absorption (Sect. 2.2.1), Compton scattering (Sect. 2.2.2), and pair production (Sect. 2.2.3). As illustrated in Fig. 2.1, photoabsorption constitutes the largest contribution to the total cross section at low photon energies, pair production is the most frequent interaction at high energies, and Compton scattering dominates in the intermediate energy range.

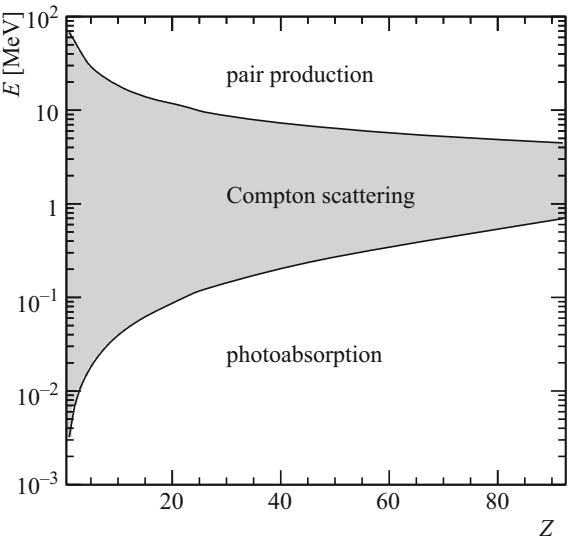

Fig. 2.1 The lower curve shows, as a function of the atomic number Z of the target material, the photon energy E below which photoelectric absorption is the most probable interaction mechanism, while the upper curve shows the energy above which pair production is the most important process. The shaded region between the two curves corresponds to the domain where Compton scattering dominates. The cross sections are taken from the NIST XCOM database [24]

Detailed descriptions of these processes can be found, for instance, in Refs. [8–10, 12, 22, 23]. The focus of this section is on photoabsorption, the description of which (as will be discussed in Sect. 2.3) is related to that of inelastic charged particle collisions in the regime of low momentum transfer.

2.2.1 Photoabsorption

In a photoelectric absorption interaction, the incident photon disappears and its energy is transferred to the target atom (or group of atoms). The intensity I of a monochromatic beam of photons with energy E thus decreases exponentially as a function of the penetration depth x in a material,

$$I(x) = I_0 \mathrm{e}^{-\mu x},$$

where the attenuation coefficient μ is proportional to the atomic density N of the medium and the photoabsorption cross section σ_γ,

$$\mu(E) = N\sigma_\gamma(E).$$

Let us first consider a (dipole-allowed) transition between the ground state $|0\rangle$ of an atom and a discrete excited state $|n\rangle$ with excitation energy E_n. The integral photoabsorption cross section of the line is given by

$$\int \sigma_\gamma^{(n)}(E)\,\mathrm{d}E = \frac{2\pi^2\alpha(\hbar c)^2}{mc^2} f_n.$$

The dimensionless quantity

$$f_n = \frac{2mc^2}{3\,(\hbar c)^2} E_n |\langle n| \sum_{j=1}^{Z} \mathbf{r}_i |0\rangle|^2, \tag{2.3}$$

with the sum extending over the electrons in the target atom, is known as the dipole oscillator strength (DOS). Similarly, transitions to the continuum are characterised by the dipole oscillator strength density $\mathrm{d}f/\mathrm{d}E$, and the photoionisation cross section $\sigma_\gamma\,(E)$ is given by

$$\sigma_\gamma\,(E) = \frac{2\pi^2\alpha\,(\hbar c)^2}{mc^2} \frac{\mathrm{d}f\,(E)}{\mathrm{d}E}. \tag{2.4}$$

The dipole oscillator strength satisfies the Thomas-Reiche-Kuhn (TRK) sum rule,

$$\sum_n f_n + \int \mathrm{d}E\, \frac{\mathrm{d}f\,(E)}{\mathrm{d}E} = Z. \tag{2.5}$$

For most gases, the contribution of excited states ($\sum f_n$) to the TRK sum rule is a few percent of the total, e.g. ~5% for argon and ~7% for methane [25, 26].

As can be seen from Fig. 2.2, the photoabsorption cross section reflects the atomic shell structure. Evaluated atomic and molecular photoabsorption cross

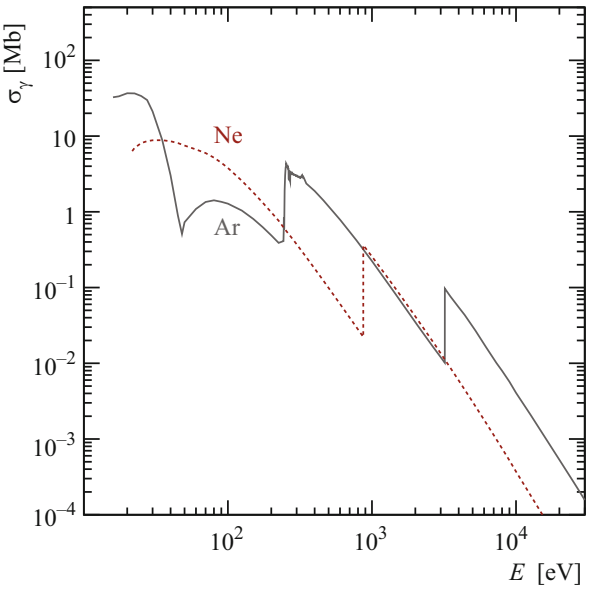

Fig. 2.2 Photoabsorption cross sections of argon (solid curve) and neon (dashed curve) as a function of the photon energy E [25, 26]

sections (both for discrete excitations as well as transitions to the continuum) for many commonly used gases are given in the book by Berkowitz [25, 26].

At energies sufficiently above the ionisation threshold, the molecular photoabsorption cross section is, to a good approximation, given by the sum of the photoabsorption cross sections of the constituent atoms. A comprehensive compilation of atomic photoabsorption data (in the energy range between ∼30 eV and 30 keV) can be found in Ref. [27]. Calculations for energies between 1 and 100 GeV are available in the NIST XCOM database [24]. Calculated photoionisation cross sections for individual shells can be found in Refs. [28–30]. At high energies, i.e. above the respective absorption edges, photons interact preferentially with inner-shell electrons. The subsequent relaxation processes (emission of fluorescence photons and Auger electrons) are discussed in Sect. 2.6.

The response of a solid with atomic number Z to an incident photon of energy $E = \hbar\omega$ is customarily described in terms of the complex dielectric function $\varepsilon(\omega) = \varepsilon_1(\omega) + \mathrm{i}\varepsilon_2(\omega)$. The oscillator strength density is related to $\varepsilon(\omega)$ by

$$\frac{\mathrm{d}f\,(E)}{\mathrm{d}E} = E\frac{2Z}{\pi\left(\hbar\Omega_p\right)^2}\frac{\varepsilon_2\,(E)}{\varepsilon_1^2\,(E)+\varepsilon_2^2\,(E)} = E\frac{2Z}{\pi\left(\hbar\Omega_p\right)^2}\mathrm{Im}\left(\frac{-1}{\varepsilon\,(E)}\right), \tag{2.6}$$

where

$$\hbar\Omega_p = \sqrt{\frac{4\pi\alpha\,(\hbar c)^3\,NZ}{mc^2}} \tag{2.7}$$

is the plasma energy of the material, which depends only on the electron density NZ. In terms of the dielectric loss function $\mathrm{Im}\,(-1/\varepsilon)$, the TRK sum rule reads

$$\int \mathrm{d}E\;\mathrm{Im}\left(\frac{-1}{\varepsilon\,(E)}\right)E = \frac{\pi}{2}\left(\hbar\Omega_p\right)^2. \tag{2.8}$$

Compilations of evaluated optical data for semiconductors are available in Ref. [32], and for solids in general in Ref. [31]. As an example, Fig. 2.3 shows the dielectric loss function of silicon, a prominent feature of which is the peak at ∼17 eV, corresponding to the plasma energy of the four valence (M-shell) electrons.

2.2.2 *Compton Scattering*

Compton scattering refers to the collision of a photon with a weakly bound electron, whereby the photon transfers part of its energy to the electron and is deflected with respect to its original direction of propagation. We assume in the following that the target electron is free and initially at rest, which is a good approximation if the photon energy E is large compared to the electron's binding energy. Due to

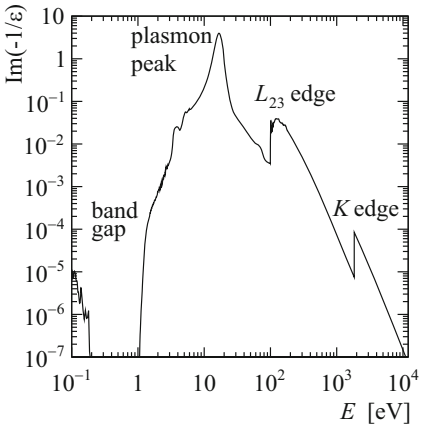

Fig. 2.3 Dielectric loss function $\mathrm{Im}\,(-1/\varepsilon\,(E))$ of solid silicon [31] as a function of the photon energy E

conservation of energy and momentum, the photon energy E' after the collision and the scattering angle θ of the photon are then related by

$$E' = \frac{mc^2}{1 - \cos\theta + (1/u)}, \tag{2.9}$$

where $u = E/\left(mc^2\right)$ is the photon energy (before the collision) in units of the electron rest energy.

The kinetic energy $T = E - E'$ imparted to the electron is largest for a head-on collision ($\theta = \pi$) and the energy spectrum of the recoil electrons consequently exhibits a cut-off (Compton edge) at

$$T_{\max} = E\frac{2u}{1+2u}.$$

The total cross section (per electron) for the Compton scattering of an unpolarised photon by a free electron at rest, derived by Klein and Nishina in 1929 [33], is given by

$$\sigma^{(\mathrm{KN})} = 2\pi\left(\frac{\alpha\hbar c}{mc^2}\right)^2\left(\frac{1+u}{u^2}\left[\frac{2\,(1+u)}{1+2u} - \frac{\ln\,(1+2u)}{u}\right] + \frac{\ln\,(1+2u)}{2u} - \frac{1+3u}{(1+2u)^2}\right). \tag{2.10}$$

At low energies ($u \ll 1$), the Klein-Nishina formula (2.10) is conveniently approximated by the expansion [34]

$$\sigma^{(\mathrm{KN})} = \underbrace{\frac{8\pi}{3}\left(\frac{\alpha\hbar c}{mc^2}\right)^2}_{\text{Thomson cross section}} \frac{1}{(1+2u)^2}\left(1 + 2u + \frac{6}{5}u^2 + \ldots\right),$$

while at high energies ($u \gg 1$) the approximation [8, 10, 22]

$$\sigma^{(\mathrm{KN})} \sim \pi \left(\frac{\alpha\hbar c}{mc^2}\right)^2 \frac{1}{u}\left(\ln(2u) + \frac{1}{2}\right)$$

can be used.

The angular distribution of the scattered photon is given by the differential cross section

$$\frac{\mathrm{d}\sigma^{(\mathrm{KN})}}{\mathrm{d}(\cos\theta)} = \pi \left(\frac{\alpha\hbar c}{mc^2}\right)^2 \left[\frac{1}{1+u(1-\cos\theta)}\right]^2 \left(\frac{1+\cos^2\theta}{2}\right) \times \left(1 + \frac{u^2(1-\cos\theta)^2}{(1+\cos^2\theta)[1+u(1-\cos\theta)]}\right),$$

which corresponds to a kinetic energy spectrum [22]

$$\frac{\mathrm{d}\sigma^{(\mathrm{KN})}}{\mathrm{d}T} = \pi \left(\frac{\alpha\hbar c}{mc^2}\right)^2 \frac{1}{u^2 mc^2}\left(2 + \left(\frac{T}{E-T}\right)^2 \left[\frac{1}{u^2} + \frac{E-T}{E} - \frac{2(E-T)}{uT}\right]\right)$$

of the target electron.

The cross section for Compton scattering off an atom scales roughly with the number of electrons in the atom and, assuming that the photon energy is large compared to the atomic binding energies, may be approximated by

$$\sigma^{(\mathrm{Compton})} \sim Z\sigma^{(\mathrm{KN})}.$$

Methods for including the effects of the binding energy and the internal motion of the orbital electrons in calculations of atomic Compton scattering cross sections are discussed, for instance, in Ref. [35].

2.2.3 *Pair Production*

For photon energies exceeding $2mc^2$, an interaction mechanism becomes possible where the incoming photon disappears and an electron-positron pair, with a total energy equal to the photon energy E, is created. Momentum conservation requires this process, which is closely related to bremsstrahlung (Sect. 2.4.1), to take place in the electric field of a nucleus or of the atomic electrons. In the latter case, kinematic constraints impose a threshold of $E > 4mc^2$.

At high photon energies, the electron-positron pair is emitted preferentially in the forward direction and the absorption coefficient due to pair production can be approximated by

$$\mu = N\sigma^{(\text{pair production})} = \frac{7}{9}\frac{1}{X_0},$$

where X_0 is a material-dependent parameter known as the radiation length (see Sect. 2.4.1). More accurate expressions are given in Ref. [8]. Tabulations of calculated pair-production cross sections can be found in Ref. [36] and are available online [24].

2.3 Interaction of Heavy Charged Particles with Matter

The main ingredient for computing the energy loss of an incident charged particle due to interactions with the electrons of the target medium is the single-differential cross section with respect to the energy transfer E in a collision. In this section, we discuss the calculation of $\mathrm{d}\sigma/\mathrm{d}E$ and its moments for "fast", point-like particles. To be precise, we consider particles with a velocity that is large compared to the velocities of the atomic electrons, corresponding to the domain of validity of the first-order Born approximation.

In the limit where the energy transfer E is large compared to the atomic binding energies, $\mathrm{d}\sigma/\mathrm{d}E$ approaches the cross section for scattering off a free electron. For a spin-zero particle with charge ze and speed βc, the asymptotic cross section (per electron) towards large energy transfers is given by [8]

$$\frac{\mathrm{d}\sigma}{\mathrm{d}E} = \underbrace{\frac{2\pi z^2 (\alpha\hbar c)^2}{mc^2\beta^2}\frac{1}{E^2}}_{\text{Rutherford cross section}}\left(1-\beta^2\frac{E}{E_{\max}}\right) = \frac{\mathrm{d}\sigma_R}{\mathrm{d}E}\left(1-\beta^2\frac{E}{E_{\max}}\right). \tag{2.11}$$

Similar expressions have been derived for particles with spin 1 and spin 1/2 [8]. The maximum energy transfer is given by the kinematics of a head-on collision between a particle with mass M and an electron (mass m) at rest,

$$E_{\max} = 2mc^2\beta^2\gamma^2\left(1+2\gamma\frac{m}{M}+\left(\frac{m}{M}\right)^2\right)^{-1}, \tag{2.12}$$

which for $M \gg m$ becomes $E_{\max} \sim 2mc^2\beta^2\gamma^2$.

These so-called "close" or "knock-on" collisions, in which the projectile interacts with a single atomic electron, contribute a significant fraction (roughly half) to the average energy loss of a charged particle in matter but are rare compared to "distant" collisions in which the particle interacts with the atom as a whole or with a group of

atoms. For an accurate calculation of $\mathrm{d}\sigma/\mathrm{d}E$, the electronic structure of the target medium therefore needs to be taken into account.

In the non-relativistic first-order Born approximation, the transition of an atom from its ground state to an excited state $|n\rangle$ involving a momentum transfer $\mathbf{q}$ is characterised by the matrix element (inelastic form factor)

$$F_{n0}(\mathbf{q}) = \langle n| \sum_{j=1}^{Z} \exp\left(\frac{\mathrm{i}}{\hbar}\mathbf{q}\cdot\mathbf{r}_j\right)|0\rangle,$$

which is independent of the projectile. The differential cross section with respect to the recoil parameter $Q = q^2/(2m)$, derived by Bethe in 1930 [16], is given by [1–3, 16]

$$\frac{\mathrm{d}\sigma_n}{\mathrm{d}Q} = \frac{2\pi z^2 (\alpha\hbar c)^2}{mc^2\beta^2}\frac{1}{Q^2}|F_{n0}(\mathbf{q})|^2 = \frac{2\pi z^2 (\alpha\hbar c)^2}{mc^2\beta^2}\frac{f_n(q)}{QE_n},$$

where $f_n(q)$ denotes the generalised oscillator strength (GOS). In the limit $q \to 0$ it becomes the dipole oscillator strength f_n discussed in Sect. 2.2.1. The double-differential cross section for transitions to the continuum (i.e. ionisation) is given by

$$\frac{\mathrm{d}^2\sigma}{\mathrm{d}E\mathrm{d}Q} = \frac{2\pi z^2 (\alpha\hbar c)^2}{mc^2\beta^2}\frac{1}{QE}\frac{\mathrm{d}f(E,q)}{\mathrm{d}E}, \tag{2.13}$$

where $\mathrm{d}f(E,q)/\mathrm{d}E$ is the generalised oscillator strength density. The GOS is constrained by the Bethe sum rule [2, 16] (a generalisation of the TRK sum rule),

$$\sum_n f_n(q) + \int \mathrm{d}E \frac{\mathrm{d}f(E,q)}{\mathrm{d}E} = Z, \quad \forall q. \tag{2.14}$$

Closed-form expressions for the generalised oscillator strength (density) exist only for very simple systems such as the hydrogen atom (Fig. 2.4). Numerical calculations are available for a number of atoms and molecules (see e.g. Ref. [37]). A prominent feature of the generalised oscillator strength density is the so-called "Bethe ridge": at high momentum transfers $\mathrm{d}f(E,q)/\mathrm{d}E$ is concentrated along the free-electron dispersion relation $Q = E$.

In order to calculate $\mathrm{d}\sigma/\mathrm{d}E$, we need to integrate the double-differential cross-section over Q,

$$\frac{\mathrm{d}\sigma}{\mathrm{d}E} = \int_{Q_{\min}}^{Q_{\max}} \mathrm{d}Q \frac{\mathrm{d}^2\sigma}{\mathrm{d}E\mathrm{d}Q}, \qquad Q_{\min} \sim \frac{E^2}{2m\beta^2c^2}. \tag{2.15}$$

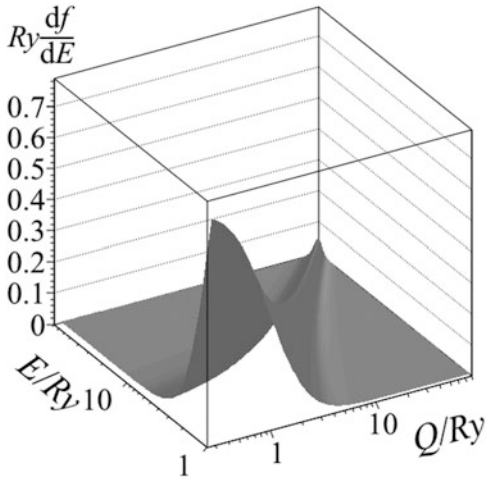

Fig. 2.4 Generalised oscillator strength density $\mathrm{d}f\,(E,q)\,/\mathrm{d}E$ of atomic hydrogen [2, 3, 16], for transitions to the continuum

For this purpose, it is often sufficient to use simplified models of the generalised oscillator strength density, based on the guidelines provided by model systems like the hydrogen atom, and using (measured) optical data in the low-Q regime.

Equation (2.13) describes the interaction of a charged particle with an isolated atom, which is a suitable approximation for a dilute gas. In order to extend it to dense media and to incorporate relativistic effects, it is convenient to use a semi-classical formalism [19, 38]. In this approach, which can be shown to be equivalent to the first-order quantum mechanical result, the response of the medium to the incident particle is described in terms of the complex dielectric function.

2.3.1 Dielectric Theory

Revisiting the energy loss of charged particles in matter from the viewpoint of classical electrodynamics, we calculate the electric field of a point charge ze moving with a constant velocity $\boldsymbol{\beta}c$ through an infinite, homogeneous and isotropic medium, that is we solve Maxwell's equations

$$\nabla\cdot\mathbf{B}=0\,,\qquad \nabla\times\mathbf{E}=-\frac{1}{c}\frac{\partial\mathbf{B}}{\partial t},$$
$$\nabla\times\mathbf{B}=\frac{1}{c}\frac{\partial\mathbf{D}}{\partial t}+\frac{4\pi}{c}\mathbf{j}\,,\qquad \nabla\cdot\mathbf{D}=4\pi\rho,$$

for source terms

$$\rho=ze\delta^3\left(\mathbf{r}-\boldsymbol{\beta}ct\right),\qquad \mathbf{j}=\boldsymbol{\beta}c\rho.$$

The perturbation due to the moving charge is assumed to be weak enough such that there is a linear relationship between the Fourier components of the electric field $\mathbf{E}$ and the displacement field $\mathbf{D}$,

$$\mathbf{D}(\mathbf{k},\omega) = \varepsilon(\mathbf{k},\omega)\,\mathbf{E}(\mathbf{k},\omega),$$

where $\varepsilon(\mathbf{k},\omega) = \varepsilon_1(\mathbf{k},\omega) + \mathrm{i}\varepsilon_2(\mathbf{k},\omega)$ is the (generalized) complex dielectric function.

The particle experiences a force $ze\mathbf{E}(\mathbf{r} = \boldsymbol{\beta}ct, t)$ that slows it down, and the stopping power is given by the component of this force parallel to the particle's direction of motion,

$$\frac{\mathrm{d}E}{\mathrm{d}x} = ze\mathbf{E}\cdot\frac{\boldsymbol{\beta}}{\beta}.$$

Adopting the Coulomb gauge $\mathbf{k}\cdot\mathbf{A} = 0$, one obtains after integrating over the angles (assuming that the dielectric function ε is isotropic),

$$\frac{\mathrm{d}E}{\mathrm{d}x} = -\frac{2z^2e^2}{\beta^2\pi}\int \mathrm{d}\omega \int \mathrm{d}k \times\left[\frac{\omega}{kc^2}\mathrm{Im}\left(\frac{-1}{\varepsilon(k,\omega)}\right) + \omega k\left(\beta^2 - \frac{\omega^2}{k^2c^2}\right)\mathrm{Im}\left(\frac{1}{-k^2c^2 + \varepsilon(k,\omega)\,\omega^2}\right)\right]. \tag{2.16}$$

The first term in the integrand represents the non-relativistic contribution to the energy loss which we would have obtained by considering only the scalar potential ϕ. It is often referred to as the longitudinal term. The second term, known as the transverse term, originates from the vector potential $\mathbf{A}$ and incorporates relativistic effects.

On a microscopic level, the energy transfer from the particle to the target medium proceeds through discrete collisions with energy transfer $E = \hbar\omega$ and momentum transfer $q = \hbar k$. Comparing Eq. (2.2) with the macroscopic result (2.16), one obtains

$$\frac{\mathrm{d}^2\sigma}{\mathrm{d}E\mathrm{d}q} = \frac{2z^2\alpha}{\beta^2\pi\hbar cN} \times\left[\frac{1}{q}\mathrm{Im}\left(\frac{-1}{\varepsilon(q,E)}\right) + \frac{1}{q}\left(\beta^2 - \frac{E^2}{q^2c^2}\right)\mathrm{Im}\left(\frac{1}{-1 + \varepsilon(q,E)\,E^2/\left(q^2c^2\right)}\right)\right]. \tag{2.17}$$

The loss function $\mathrm{Im}\left(-1/\varepsilon\left(q,E\right)\right)$ and the generalized oscillator strength density are related by

$$\frac{\mathrm{d}f\left(E,q\right)}{\mathrm{d}E}=E\frac{2Z}{\pi\left(\hbar\Omega_p\right)^2}\mathrm{Im}\left(\frac{-1}{\varepsilon\left(q,E\right)}\right). \tag{2.18}$$

Using this identity, we see that the longitudinal term (first term) in Eq. (2.17) is equivalent to the non-relativistic quantum mechanical result (2.13). As is the case with the generalized oscillator strength density, closed-form expressions for the dielectric loss function $\mathrm{Im}\left(-1/\varepsilon\left(q,E\right)\right)$ can only be derived for simple systems like the ideal Fermi gas [39, 40]. In the following (Sects. 2.3.2 and 2.3.3), we discuss two specific models of $\mathrm{Im}\left(-1/\varepsilon\left(q,E\right)\right)$ (or, equivalently, $\mathrm{d}f\left(E,q\right)/\mathrm{d}E$).

2.3.2 Bethe-Fano Method

The relativistic version of Eq. (2.13) or, in other words, the equivalent of Eq. (2.17) in oscillator strength parlance, is [1, 41]

$$\frac{\mathrm{d}^2\sigma}{\mathrm{d}E\mathrm{d}Q}=\frac{2\pi z^2\left(\alpha\hbar c\right)^2}{mc^2\beta^2}Z\left[\frac{\left|F\left(E,\mathbf{q}\right)\right|^2}{Q^2\left(1+\frac{Q}{2mc^2}\right)^2}+\frac{\left|\boldsymbol{\beta}_t\cdot\mathbf{G}\left(E,\mathbf{q}\right)\right|^2}{\left[Q\left(1+\frac{Q}{2mc^2}\right)-\frac{E^2}{2mc^2}\right]^2}\right]\left(1+\frac{Q}{mc^2}\right) \tag{2.19}$$

where $Q\left(1+Q/2mc^2\right)=q^2/2m$, $\boldsymbol{\beta}_t$ is the component of the velocity perpendicular to the momentum transfer $\mathbf{q}$, and $F\left(E,\mathbf{q}\right)$ and $\mathbf{G}\left(E,\mathbf{q}\right)$ represent the matrix elements for longitudinal and transverse excitations.

Depending on the type of target and the range of momentum transfers involved, we can use Eqs. (2.13), (2.19) or (2.17) as a starting point for evaluating the single-differential cross section. Following the approach described by Fano [1], we split $\mathrm{d}\sigma/\mathrm{d}E$ in four parts. For small momentum transfers ($Q<Q_1\sim 1\,\mathrm{Ry}$), we can use the non-relativistic expression (2.13) for the longitudinal term and approximate the generalised oscillator strength density by its dipole limit,

$$\frac{\mathrm{d}\sigma^{(1)}}{\mathrm{d}E}=\frac{2\pi z^2\left(\alpha\hbar c\right)^2}{mc^2\beta^2}\frac{1}{E}\frac{\mathrm{d}f\left(E\right)}{\mathrm{d}E}\int_{Q_{\min}}^{Q_1}\frac{\mathrm{d}Q}{Q}=\frac{2\pi z^2\left(\alpha\hbar c\right)^2}{mc^2\beta^2}\frac{1}{E}\frac{\mathrm{d}f\left(E\right)}{\mathrm{d}E}\ln\frac{Q_1 2mc^2\beta^2}{E^2}. \tag{2.20}$$

In terms of the dielectric loss function, one obtains

$$\frac{\mathrm{d}\sigma^{(1)}}{\mathrm{d}E}=\frac{z^2\alpha}{\beta^2\pi\hbar cN}\mathrm{Im}\left(\frac{-1}{\varepsilon\left(E\right)}\right)\ln\frac{Q_1 2mc^2\beta^2}{E^2}.$$

For high momentum transfers ($Q > Q_2 \sim 30\,\mathrm{keV}$), i.e. for close collisions where the binding energy of the atomic electrons can be neglected, the longitudinal and transverse matrix elements are strongly peaked at the Bethe ridge $Q = E$. Using [1]

$$|F(E,\mathbf{q})|^2 \sim \frac{1 + Q/\left(2mc^2\right)}{1 + Q/\left(mc^2\right)}\delta(E-Q),$$

$$|\boldsymbol{\beta}_t \cdot \mathbf{G}(E,\mathbf{q})|^2 \sim \beta_t^2 \frac{1 + Q/\left(2mc^2\right)}{1 + Q/\left(mc^2\right)}\delta(E-Q)$$

and

$$\beta_t^2 = \frac{1}{1 + Q/\left(2mc^2\right)} - \left(1-\beta^2\right)$$

one obtains (for longitudinal and transverse excitations combined),

$$\frac{\mathrm{d}\sigma^{(h)}}{\mathrm{d}E} = \frac{2\pi z^2 (\alpha\hbar c)^2}{mc^2\beta^2}\frac{Z}{E}\left(1 - \frac{E\left(1-\beta^2\right)}{2mc^2}\right). \tag{2.21}$$

In the intermediate range, $Q_1 < Q < Q_2$, numerical calculations of the generalised oscillator strength density are used. An example of $\mathrm{d}f(E,q)/\mathrm{d}E$ is shown in Fig. 2.5. Since the limits Q_1, Q_2 do not depend on the particle velocity, the integrals

$$\frac{\mathrm{d}\sigma^{(2)}}{\mathrm{d}E} = \frac{2\pi z^2 (\alpha\hbar c)^2}{mc^2\beta^2}\frac{1}{E}\int_{Q_1}^{Q_2}\frac{\mathrm{d}Q}{Q}\frac{\mathrm{d}f(E,q)}{\mathrm{d}E}$$

need to be evaluated only once for each value of E. The transverse contribution can be neglected[1] [41].

The last contribution, described in detail in Ref. [1], is due to low-Q transverse excitations in condensed matter. Setting $\mathrm{Im}\left(-1/\varepsilon(E,q)\right) = \mathrm{Im}\left(-1/\varepsilon(E)\right)$ in the second term in Eq. (2.17) and integrating over q gives

$$\frac{\mathrm{d}\sigma^{(3)}}{\mathrm{d}E} = \frac{z^2\alpha}{\beta^2\pi N\hbar c} \times\left[\mathrm{Im}\left(\frac{-1}{\varepsilon(E)}\right)\ln\frac{1}{\left|1-\beta^2\varepsilon(E)\right|} + \left(\beta^2 - \frac{\varepsilon_1(E)}{|\varepsilon(E)|^2}\right)\left(\frac{\pi}{2} - \arctan\frac{1-\beta^2\varepsilon_1(E)}{\beta^2\varepsilon_2(E)}\right)\right]. \tag{2.22}$$

[1] For particle speeds $\beta < 0.1$, this approximation will cause errors, especially for M_0.

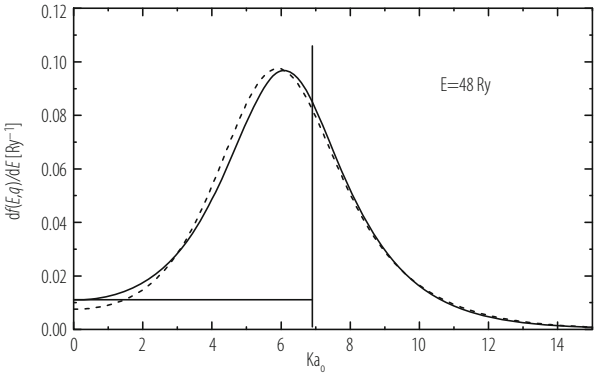

Fig. 2.5 Generalized oscillator strength density for Si for an energy transfer $E = 48\,\mathrm{Ry}$ to the 2p-shell electrons [41–44], as function of ka_0 (where $k^2a_0^2 = Q/\mathrm{Ry}$). Solid line: calculated with Herman-Skilman potential, dashed line: hydrogenic approximation [45, 46]. The horizontal and vertical line define the FVP approximation (Sect. 2.3.3)

We will discuss this term in more detail in Sect. 2.3.3. The total single-differential cross section,

$$\frac{\mathrm{d}\sigma}{\mathrm{d}E} = \frac{\mathrm{d}\sigma^{(1)}}{\mathrm{d}E} + \frac{\mathrm{d}\sigma^{(2)}}{\mathrm{d}E} + \frac{\mathrm{d}\sigma^{(3)}}{\mathrm{d}E} + \frac{\mathrm{d}\sigma^{(h)}}{\mathrm{d}E},$$

is shown in Fig. 2.6 for particles with $\beta\gamma = 4$ in silicon which, at present, is the only material for which calculations based on the Bethe-Fano method are available.

2.3.3 *Fermi Virtual-Photon (FVP) Method*

In the Bethe-Fano algorithm discussed in the previous section, the dielectric function $\varepsilon\,(q, E)$ was approximated at low momentum transfer by its optical limit $\varepsilon\,(E)$. In the Fermi virtual-photon (FVP) or Photoabsorption Ionisation (PAI) model [6, 47, 48], this approximation is extended to the entire domain $q^2 < 2mE$. Guided by the shape of the hydrogenic GOS, the remaining contribution to $\mathrm{Im}\,(-1/\varepsilon\,(q, E))$ required to satisfy the Bethe sum rule

$$\int_0^\infty E\,\mathrm{Im}\left(\frac{-1}{\varepsilon\,(q, E)}\right)\mathrm{d}E = \frac{\pi}{2}\left(\hbar\Omega_p\right)^2 \quad \forall q, \tag{2.23}$$

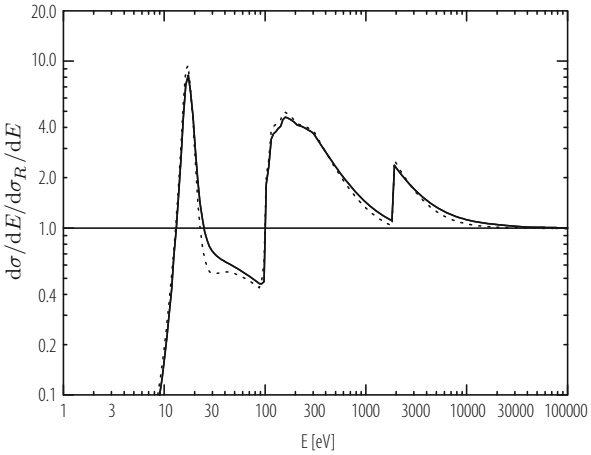

Fig. 2.6 Differential cross section $\mathrm{d}\sigma/\mathrm{d}E$, divided by the Rutherford cross section $\mathrm{d}\sigma_R/\mathrm{d}E$, for particles with $\beta\gamma = 4$ in silicon, calculated with two methods. The abscissa is the energy loss E in a single collision. The Rutherford cross section is represented by the horizontal line at 1.0. The solid line was obtained [41] with the Bethe-Fano method (Sect. 2.3.2). The cross section calculated with the FVP method (Sect. 2.3.3) is shown by the dotted line. The functions all extend to $E_{\max} \sim 16\,\mathrm{MeV}$. The moments are $M_0 = 4$ collisions/μm and $M_1 = 386\,\mathrm{eV/\mu m}$ (Table 2.2)

is attributed to the scattering off free electrons (close collisions). This term is thus of the form $C\delta\left(E - q^2/(2m)\right)$, with the factor C being determined by the normalisation (2.23),

$$C = \frac{1}{E}\int_0^E E'\mathrm{Im}\left(\frac{-1}{\varepsilon\left(E'\right)}\right)\mathrm{d}E'.$$

Combining the two terms, the longitudinal loss function becomes

$$\mathrm{Im}\left(\frac{-1}{\varepsilon\left(q,\,E\right)}\right) = \mathrm{Im}\left(\frac{-1}{\varepsilon\left(E\right)}\right)\Theta\left(E - \frac{q^2}{2m}\right) + \frac{\delta\left(E - \frac{q^2}{2m}\right)}{E}\int_0^E E'\mathrm{Im}\left(\frac{-1}{\varepsilon\left(E'\right)}\right)\mathrm{d}E'.$$

In the transverse term, the largest contribution to the integral comes from the region $E \sim qc/\sqrt{\varepsilon}$, i.e. from the vicinity of the (real) photon dispersion relation, and one consequently approximates $\varepsilon\left(q,\,E\right)$ by $\varepsilon\left(E\right)$ throughout.

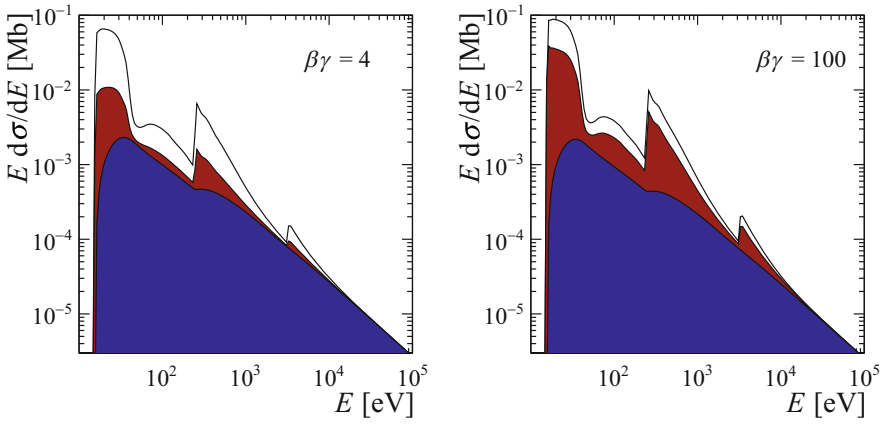

Fig. 2.7 Differential cross section $\mathrm{d}\sigma/\mathrm{d}E$ (scaled by the energy loss E) calculated using the FVP algorithm, for particles with $\beta\gamma = 4$ (left) and $\beta\gamma = 100$ (right) in argon (at atmospheric pressure, $T = 20\,^{\circ}\mathrm{C}$). The upper, unshaded area corresponds to the first term in Eq. (2.24), i.e. to the contribution from distant longitudinal collisions. The lower area corresponds to the contribution from close longitudinal collisions, given by the second term in Eq. (2.24). The intermediate area corresponds to the contribution from transverse collisions

The integration over q can then be carried out analytically and one obtains for the single-differential cross section $\mathrm{d}\sigma/\mathrm{d}E$

$$\frac{\mathrm{d}\sigma}{\mathrm{d}E} = \frac{z^2\alpha}{\beta^2\pi N\hbar c}\left[\mathrm{Im}\left(\frac{-1}{\varepsilon\,(E)}\right)\ln\frac{2mc^2\beta^2}{E} + \frac{1}{E^2}\int_0^E E'\mathrm{Im}\left(\frac{-1}{\varepsilon\,(E')}\right)\mathrm{d}E'\right] + \frac{z^2\alpha}{\beta^2\pi N\hbar c}$$
$$\times\left[\mathrm{Im}\left(\frac{-1}{\varepsilon\,(E)}\right)\ln\frac{1}{\left|1-\beta^2\varepsilon\,(E)\right|} + \left(\beta^2 - \frac{\varepsilon_1\,(E)}{|\varepsilon\,(E)|^2}\right)\left(\frac{\pi}{2} - \arctan\frac{1-\beta^2\varepsilon_1\,(E)}{\beta^2\varepsilon_2\,(E)}\right)\right] \tag{2.24}$$

The relative importance of the different terms in Eq. (2.24) is illustrated in Fig. 2.7. The first two terms describe the contributions from longitudinal distant and close collisions. The contribution from transverse collisions (third and fourth term) is identical to $\mathrm{d}\sigma^{(3)}/\mathrm{d}E$ in the Bethe-Fano algorithm. As can be seen from Fig. 2.7, its importance grows with increasing $\beta\gamma$. The third term incorporates the relativistic density effect, i.e. the screening of the electric field due to the polarisation of the medium induced by the passage of the charged particle. In the transparency region $\varepsilon_2\,(E) = 0$, the fourth term can be identified with the cross section for the emission of Cherenkov photons. It vanishes for $\beta < 1/\sqrt{\varepsilon}$; above this threshold it becomes

$$\frac{\mathrm{d}\sigma^{(\mathrm{C})}}{\mathrm{d}E} = \frac{\alpha}{N\hbar c}\left(1 - \frac{1}{\beta^2\varepsilon}\right) \sim \frac{\alpha}{N\hbar c}\sin^2\theta_{\mathrm{C}},$$

where

$$\cos\theta_{\mathrm{C}} = \frac{1}{\beta\sqrt{\varepsilon}}.$$

Cherenkov detectors are discussed in detail in Chap. 7 of this book.

In the formulation of the PAI model by Allison and Cobb [6], the imaginary part ε_2 of the dielectric function is approximated by the photoabsorption cross section σ_γ,

$$\varepsilon_2(E) \sim \frac{N\hbar c}{E}\sigma_\gamma(E) \tag{2.25}$$

and the real part ε_1 is calculated from the Kramers-Kronig relation

$$\varepsilon_1(E) - 1 = \frac{2}{\pi}\mathsf{P}\int_0^\infty \frac{E'\varepsilon_2(E')}{E'^2 - E^2}\mathrm{d}E'.$$

In addition, the approximation $|\varepsilon(E)|^2 \sim 1$ is used. These are valid approximations if the refractive index[2] is close to one ($\mathsf{n} \sim 1$) and the attenuation coefficient k is small. For gases, this requirement is usually fulfilled for energies above the ionisation threshold.

Requiring only optical data as input, the FVP/PAI model is straightforward to implement in computer simulations. In the HEED program [49], the differential cross section $\mathrm{d}\sigma/\mathrm{d}E$ is split into contributions from each atomic shell, which enables one to simulate not only the energy transfer from the projectile to the medium but also the subsequent atomic relaxation processes (Sect. 2.6). The GEANT4 implementation of the PAI model is described in Ref. [50]. For reasons of computational efficiency, the photoabsorption cross section $\sigma_\gamma(E)$ is parameterised as a fourth-order polynomial in $1/E$. FVP calculations for Ne and Ar/CH_4 (90:10) are discussed in Ref. [51].

2.3.4 *Integral Quantities*

For validating and comparing calculations of the differential cross section, it is instructive to consider the moments M_i of $N\mathrm{d}\sigma/\mathrm{d}E$, in particular the inverse mean free path M_0 and the stopping power M_1.

[2]The complex refractive index and the dielectric function are related by $\mathsf{n} + \mathrm{i}\mathsf{k} = \sqrt{\varepsilon}$.

2.3.4.1 Inverse Mean Free Path

In the relativistic first-order Born approximation, the inverse mean free path for ionising collisions has the form [1, 2]

$$M_0 = \frac{2\pi z^2 (\alpha\hbar c)^2}{mc^2\beta^2} N \left[M^2 \left(\ln\left(\beta^2\gamma^2\right) - \beta^2 \right) + C \right], \tag{2.26}$$

where

$$M^2 = \int \frac{1}{E} \frac{\mathrm{d}f\,(E)}{\mathrm{d}E} \mathrm{d}E, \qquad C = M^2 \left(\ln \tilde{c} + \ln \frac{4}{\alpha^2} \right),$$

and $\tilde{c}$ is a material-dependent parameter that can be calculated from the generalised oscillator strength density. Calculations can be found, for example, in Refs. [53, 54]. As in the Bethe stopping formula (2.28) discussed below, a correction term can be added to Eq. (2.26) to account for the density effect [55].

The inverse mean free path for dipole-allowed discrete excitations is given by [2]

$$M_0^{(n)} = \frac{2\pi z^2 (\alpha\hbar c)^2}{mc^2\beta^2} N \frac{f_n}{E_n} \left[\ln\left(\beta^2\gamma^2\right) - \beta^2 + \ln \tilde{c}_n + \ln \frac{4}{\alpha^2} \right].$$

We can thus obtain a rough estimate of the relative frequencies of excitations and ionising collisions from optical data. In argon, for instance, the ratio of $\sum f_n/E_n$ and M^2 is ∼20% [25].

For gases, M_0 can be determined experimentally by measuring the inefficiency of a gas-filled counter operated at high gain ("zero-counting method"). Results (in the form of fit parameters M^2, C) from an extensive series of measurements, using electrons with kinetic energies between 0.1 and 2.7 MeV, are reported in Ref. [52]. Other sets of experimental data obtained using the same technique can be found in Refs. [56, 57]. Table 2.1 shows a comparison between measured and calculated values (using the FVP algorithm) of M_0 for particles with $\beta\gamma = 3.5$ at a temperature of 20 °C and atmospheric pressure. The inverse mean free path is

Table 2.1 Measurements [52] and calculations (using the FVP algorithm as implemented in HEED [49]) of M_0 for $\beta\gamma = 3.5$ at $T = 20\,^{\circ}\mathrm{C}$ and atmospheric pressure

	M_0 [cm^{-1}]	
Gas	Measurement	FVP
Ne	10.8	10.5
Ar	23.0	25.4
Kr	31.5	31.0
Xe	43.2	42.1
CO_2	34.0	34.0
CF_4	50.9	51.8
CH_4	24.6	29.4
iC_4H_{10}	83.4	90.9

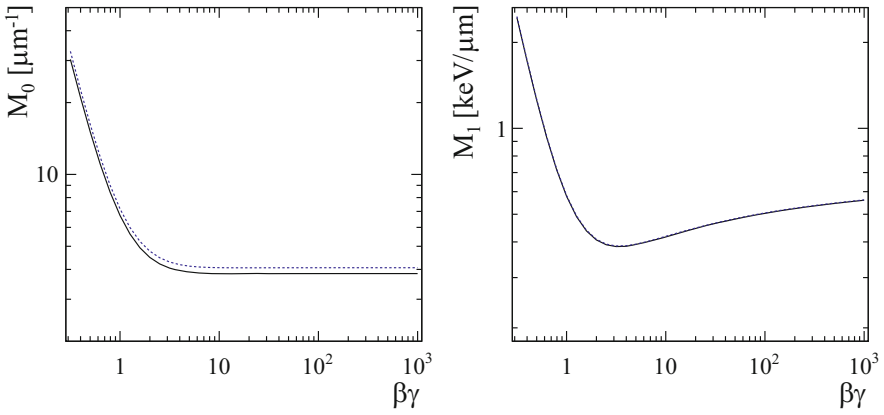

Fig. 2.8 Inverse ionisation mean free path (left) and stopping power (right) of heavy charged particles in silicon as a function of $\beta\gamma$, calculated using the Bethe-Fano algorithm (solid line) and the FVP model (dashed line). The two stopping power curves are virtually identical

sensitive to the detailed shape of the differential cross section $\mathrm{d}\sigma/\mathrm{d}E$ at low energies and, consequently, to the optical data used.

Figure 2.8(left) shows M_0 in solid silicon as a function of $\beta\gamma$, calculated using the Bethe-Fano and FVP algorithms. The difference between the results is $\sim 6-8\%$, as can also be seen from Table 2.2. Owing to the more detailed (and more realistic) modelling of the generalised oscillator strength density at intermediate Q, the Bethe-Fano algorithm can be expected to be more accurate than the FVP method.

2.3.4.2 Stopping Power

Let us first consider the average energy loss of a non-relativistic charged particle in a dilute gas, with the double-differential cross section given by Eq. (2.13),

$$-\frac{\mathrm{d}E}{\mathrm{d}x} = \frac{2\pi z^2 (\alpha\hbar c)^2}{mc^2\beta^2} N \int_{E_{\min}}^{E_{\max}} \mathrm{d}E \int_{Q_{\min}}^{Q_{\max}} \frac{\mathrm{d}Q}{Q} \frac{\mathrm{d}f(E,q)}{\mathrm{d}E}.$$

As an approximation, we assume that the integrations over Q and E can be interchanged and the integration limits $Q_{\min}, Q_{\max}$ (which depend on E) be replaced by average values $\overline{Q}_{\min} = I^2/\left(2m\beta^2c^2\right)$, $\overline{Q}_{\max} = E_{\max}$ [58]. Using the Bethe sum rule (2.23), we then obtain

$$-\frac{\mathrm{d}E}{\mathrm{d}x} = \frac{2\pi z^2 (\alpha\hbar c)^2}{mc^2\beta^2} NZ \ln \frac{2mc^2\beta^2 E_{\max}}{I^2},$$

where the target medium is characterised by a single parameter: the "mean ionisation energy" I, defined by

$$\ln I = \frac{1}{Z}\int \mathrm{d}E \ln E \frac{\mathrm{d}f\,(E)}{\mathrm{d}E}$$

in terms of the dipole oscillator strength density, or

$$\ln I = \frac{2}{\pi\left(\hbar\Omega_p\right)^2}\int \mathrm{d}E\; E\,\mathrm{Im}\left(\frac{-1}{\varepsilon\,(E)}\right)\ln E. \tag{2.27}$$

in terms of the dielectric loss function.

In the relativistic case, one finds the well-known Bethe stopping formula

$$-\frac{\mathrm{d}E}{\mathrm{d}x} = \frac{2\pi z^2\,(\alpha\hbar c)^2}{mc^2\beta^2} NZ\left[\ln\frac{2mc^2\beta^2\gamma^2 E_{\max}}{I^2} - 2\beta^2 - \delta\right], \tag{2.28}$$

where δ is a correction term accounting for the density effect [59].

Sets of stopping power tables for protons and alpha particles are available in ICRU report 49 [60] and in the PSTAR and ASTAR online databases [61]. Tables for muons are given in Ref. [62]. These tabulations include stopping power contributions beyond the first-order Born approximation, such as shell corrections [42, 45, 46] and the Barkas-Andersen effect [63–65].

The stopping power in silicon obtained from the Bethe-Fano algorithm (Sect. 2.3.2) has been found to agree with measurements within ±0.5% [41]. As can be seen from Table 2.2 and Fig. 2.8, FVP and Bethe-Fano calculations for M_1 in silicon are in close agreement, with differences <1%.

In addition to M_0, M_1, Table 2.2 also includes the most probable value of the energy loss spectrum in an 8 µm thick layer of silicon. For thin absorbers, as will be discussed in Sect. 2.5, the stopping power $\mathrm{d}E/\mathrm{d}x$ is not a particularly meaningful quantity for characterising energy loss spectra. Because of the asymmetric shape of the differential cross section $\mathrm{d}\sigma/\mathrm{d}E$, the most probable value Δ_p of the energy loss distribution is typically significantly smaller than the average energy loss $\langle\Delta\rangle = M_1 x$.

2.4 Electron Collisions and Bremsstrahlung

The formalism for computing the differential cross section $\mathrm{d}\sigma/\mathrm{d}E$ for collisions of heavy charged particles with the electrons of the target medium, discussed in Sect. 2.3, is also applicable to electron and positron projectiles, except that the asymptotic close-collision cross section (2.11) is replaced by the Møller and Bhabha cross sections respectively [8, 66]. When evaluating the inverse mean free path M_0 or the stopping power M_1, we further have to take into account that the energy loss

Table 2.2 Integral properties of collision cross sections for Si calculated with Bethe-Fano (B-F) and FVP algorithms

	M_0 [μm^{-1}]		M_1 [eV/μm]		Δ_p/x [eV/μm]	
$\beta\gamma$	B-F	FVP	B-F	FVP	B-F	FVP
0.316	30.325	32.780	2443.72	2465.31	1677.93	1722.92
0.398	21.150	22.781	1731.66	1745.57	1104.90	1135.68
0.501	15.066	16.177	1250.93	1260.18	744.60	765.95
0.631	11.056	11.840	928.70	935.08	520.73	536.51
0.794	8.433	9.010	716.37	720.98	381.51	394.03
1.000	6.729	7.175	578.29	581.79	294.54	304.89
1.259	5.632	5.996	490.84	493.65	240.34	249.25
1.585	4.932	5.245	437.34	439.72	207.15	215.02
1.995	4.492	4.771	406.59	408.70	187.39	194.60
2.512	4.218	4.476	390.95	392.89	176.30	183.06
3.162	4.051	4.296	385.29	387.12	170.70	177.16
3.981	3.952	4.189	386.12	387.89	168.59	174.81
5.012	3.895	4.127	391.08	392.80	168.54	174.63
6.310	3.865	4.094	398.54	400.24	169.62	175.60
7.943	3.849	4.076	407.39	409.07	171.19	177.10
10.000	3.842	4.068	416.91	418.58	172.80	178.66
12.589	3.839	4.064	426.63	428.29	174.26	180.06
15.849	3.839	4.063	436.30	437.96	175.45	181.24
19.953	3.839	4.063	445.79	447.44	176.36	182.14
25.119	3.840	4.063	455.03	456.68	177.04	182.79
31.623	3.840	4.064	463.97	465.63	177.53	183.28
39.811	3.841	4.064	472.61	474.27	177.86	183.61
50.119	3.842	4.065	480.93	482.58	178.09	183.83
63.096	3.842	4.065	488.90	490.55	178.22	183.95
79.433	3.842	4.065	496.52	498.17	178.32	184.06
100.000	3.842	4.066	503.77	505.42	178.38	184.10
125.893	3.843	4.066	510.66	512.31	178.43	184.15
158.489	3.843	4.066	517.20	518.84	178.44	184.17
199.526	3.843	4.066	523.40	525.05	178.47	184.18
251.189	3.843	4.066	529.29	530.94	178.48	184.18
316.228	3.843	4.066	534.91	536.56	178.48	184.21
398.107	3.843	4.066	540.28	541.92	178.48	184.22
501.187	3.843	4.066	545.43	547.08	178.48	184.22
630.958	3.843	4.066	550.40	552.05	178.48	184.22
794.329	3.843	4.066	555.21	556.86	178.48	184.22
1000.000	3.843	4.066	559.89	561.54	178.48	184.22

The third column shows the most probable value Δ_p of the energy loss spectrum divided by the track length x, for $x = 8\,\mu m$. The minimum values for M_0 are at $\beta\gamma \sim 18$, for M_1 at $\beta\gamma \sim 3.2$, for Δ_p at $\beta\gamma \sim 5$. The relativistic rise for M_0 is 0.1%, for M_1 it is 45%, for Δ_p it is 6%

of an electron in an ionising collision is limited to half of its kinetic energy,

$$E_{\max} = \frac{1}{2} mc^2 (\gamma - 1) , \tag{2.29}$$

as primary and secondary electron are indistinguishable. Stopping power tables for electrons are available in ICRU report 37 [67] and in the ESTAR database [61].

The other main mechanism by which fast electrons and positrons lose energy when traversing matter is the emission of radiation (bremsstrahlung) due to deflections in the electric field of the nucleus and the atomic electrons.

2.4.1 Bremsstrahlung

Let us first consider electron-nucleus bremsstrahlung, the first quantum-mechanical description of which was developed by Bethe and Heitler [68]. The differential cross section (per atom) for the production of a bremsstrahlung photon of energy E by an incident electron of kinetic energy T is given by [8, 68]

$$\frac{\mathrm{d}\sigma_{\mathrm{rad}}}{\mathrm{d}E} = 4\alpha^3 \left(\frac{\hbar c}{mc^2} \right)^2 Z^2 \frac{F(u, T)}{E}, \tag{2.30}$$

where $u = E/\left(\gamma mc^2\right)$ denotes the ratio of the photon energy to the projectile energy. Expressions for the function $F(u, T)$ are reviewed in Ref. [69] and can be fairly complex. Amongst other parameters, $F(u, T)$ depends on the extent to which the charge of the nucleus is screened by the atomic electrons. In the first-order Born approximation and in the limit of complete screening, applicable at high projectile energies, one obtains [8, 68, 69]

$$F(u) = \left(1 + (1-u)^2 - \frac{2}{3}(1-u) \right) \ln \frac{183}{Z^{1/3}} + \frac{1}{9}(1-u) . \tag{2.31}$$

The theoretical description of electron-electron bremsstrahlung is similar to the electron-nucleus case, except that the differential cross section is proportional to Z instead of Z^2. To a good approximation, we can include electron-electron bremsstrahlung in Eq. (2.30) by replacing the factor Z^2 by $Z(Z+1)$.

The inverse mean free path for the emission of a bremsstrahlung photon with energy $E > E_{\mathrm{cut}}$ is given by

$$\lambda^{-1} = M_0 = N \int_{E_{\mathrm{cut}}}^{T} \frac{\mathrm{d}\sigma_{\mathrm{rad}}}{\mathrm{d}E} \mathrm{d}E .$$

If we neglect the term $(1-u)/9$ in Eq. (2.31), we find for the radiative stopping power at $T \gg mc^2$

$$-\frac{\mathrm{d}E}{\mathrm{d}x} = M_1 = N\int_0^T E\frac{\mathrm{d}\sigma_{\mathrm{rad}}}{\mathrm{d}E}\mathrm{d}E \sim \frac{T}{X_0}, \tag{2.32}$$

where the parameter X_0, defined by

$$\frac{1}{X_0} = 4\alpha^3\left(\frac{\hbar c}{mc^2}\right)^2 NZ\,(Z+1)\ln\frac{183}{Z^{1/3}}, \tag{2.33}$$

is known as the radiation length. Values of X_0 for many commonly used materials can be found in Ref. [70] and on the PDG webpage [71]. Silicon, for instance, has a radiation length of $X_0 \sim 9.37\,\mathrm{cm}$ [71].

Being approximately proportional to the kinetic energy of the projectile, the radiative stopping power as a function of T increases faster than the average energy loss due to ionising collisions given by Eq. (2.28). At high energies—more precisely, above a so-called critical energy ($\sim$38 MeV in case of silicon [71])—bremsstrahlung therefore represents the dominant energy loss mechanism of electrons and positrons.

2.5 Energy Losses Along Tracks: Multiple Collisions and Spectra

Consider an initially monoenergetic beam of identical particles traversing a layer of material of thickness x. Due to the randomness both in the number of collisions and in the energy loss in each of the collisions, the total energy loss Δ in the absorber will vary from particle to particle. Depending on the use case, the kinetic energy of the particles, and the thickness x, different techniques for calculating the probability distribution $f(\Delta, x)$—known as "straggling function" [72]—can be used.

Our focus in this section is on scenarios where the average energy loss in the absorber is small compared to the kinetic energy T of the incident particle (as is usually the case in vertex and tracking detectors), such that the differential cross section $\mathrm{d}\sigma/\mathrm{d}E$ and its moments do not change significantly between the particle's entry and exit points in the absorber. The number of collisions n then follows a Poisson distribution

$$p(n, x) = \frac{\langle n\rangle^n}{n!}\mathrm{e}^{-\langle n\rangle}, \tag{2.34}$$

with mean $\langle n\rangle = xM_0$. The probability $f^{(1)}(E)\,\mathrm{d}E$ for a particle to lose an amount of energy between E and $E+\mathrm{d}E$ in a single collision is given by the normalised

differential cross section,

$$f^{(1)}(E) = \frac{1}{M_0} N \frac{\mathrm{d}\sigma}{\mathrm{d}E},$$

and the probability distribution for a total energy loss Δ in n collisions is obtained from n-fold convolution of $f^{(1)}$,

$$f^{(n)}(\Delta) = \underbrace{\left(f^{(1)} \otimes f^{(1)} \otimes \cdots \otimes f^{(1)}\right)}_{n \text{ times}}(\Delta) = \int \mathrm{d}E \; f^{(n-1)}(\Delta - E)\, f^{(1)}(E),$$

as illustrated in Figs. 2.9 and 2.10.

The probability distribution for a particle to suffer a total energy loss Δ over a fixed distance x is given by [72, 73]

$$f(\Delta, x) = \sum_{n=0}^{\infty} p(n, x)\, f^{(n)}(\Delta), \tag{2.35}$$

where $f^{(0)}(\Delta) = \delta(\Delta)$. Equation (2.35) can be evaluated in a stochastic manner (Sect. 2.5.1), by means of direct numerical integration (Sect. 2.5.2), or by using integral transforms (Sect. 2.5.3).

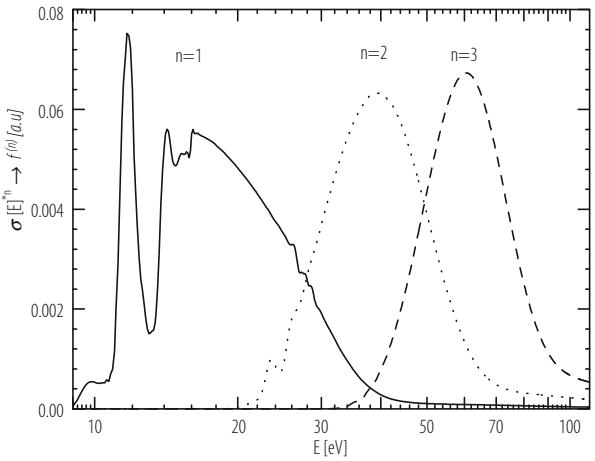

Fig. 2.9 Distributions $f^{(n)}$ of the energy loss in n collisions (n-fold convolution of the single-collision energy loss spectrum) for Ar/CH_4 (90:10)

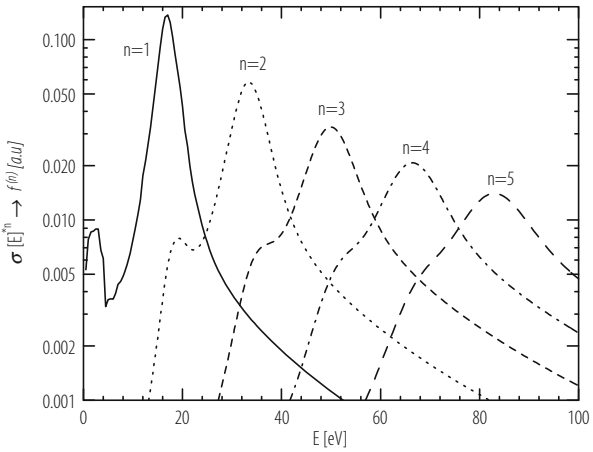

Fig. 2.10 Distributions $f^{(n)}$ of the energy loss in n collisions for solid silicon. The plasmon peak at ∼17 eV appears in each spectrum at $E \sim n \times 17$ eV, and its FWHM is proportional to $\sqrt{n}$. The structure at ∼2 eV appears at $2 + 17(n - 1)$ eV, but diminishes with increasing n. For $n = 6$ (not shown) the plasmon peak (at 102 eV) merges with the L-shell energy losses at 100 eV, also see Fig. 2.12

2.5.1 Monte Carlo Method

In a detailed Monte Carlo simulation, the trajectory of a single incident particle is followed from collision to collision. The required ingredients are the inverse mean free path $M_0^{(i)}$ and the cumulative distribution function,

$$\Phi^{(i)}(E) = \frac{1}{M_0^{(i)}} \int_0^E N \frac{\mathrm{d}\sigma^{(i)}}{\mathrm{d}E'} \mathrm{d}E', \tag{2.36}$$

for each interaction process i (electronic collisions, bremsstrahlung, etc.) to be taken into account in the simulation. The distance Δx between successive collisions follows an exponential distribution and is sampled according to

$$\Delta x = -\frac{\ln r}{\lambda^{-1}},$$

where $r \in (0, 1]$ is a uniformly distributed random number and

$$\lambda^{-1} = \sum_i M_0^{(i)}$$

is the total inverse mean free path. After updating the coordinates of the particle, the collision mechanism to take place is chosen based on the relative frequencies $M_0^{(i)}/\lambda^{-1}$. The energy loss in the collision is then sampled by drawing another uniform random variate $u \in [0, 1]$, and determining the corresponding energy loss E from the inverse of the cumulative distribution,

$$E = \Phi^{-1}(u) .$$

In general, the new direction after the collision will also have to be sampled from a suitable distribution. The above procedure is repeated until the particle has left the absorber. The spectrum $f(\Delta, x)$ is found by simulating a large number of particles and recording the energy loss Δ in a histogram. Advantages offered by the Monte Carlo approach include its straightforward implementation, the possibility of including interaction mechanisms other than inelastic scattering (bremsstrahlung, elastic scattering etc.), and the fact that it does not require approximations to the shape of $\mathrm{d}\sigma/\mathrm{d}E$ to be made.

For thick absorbers, detailed simulations can become unpractical due to the large number of collisions, and the need to update the inverse mean free path M_0 and the cumulative distribution $\Phi(E)$ following the change in velocity of the particle.

In "mixed" simulation schemes, a distinction is made between "hard" collisions which are simulated individually, and "soft" collisions (e.g. elastic collisions with a small angular deflection of the projectile, or emission of low-energy bremsstrahlung photons) the cumulative effect of which is taken into account after each hard scattering event. Details on the implementation of mixed Monte Carlo simulations can be found, for example, in the PENELOPE user guide [74].

2.5.2 Convolutions

For short track segments, one can calculate the distributions $f^{(n)}$ explicitly by numerical integration and construct $f(\Delta, x)$ directly using Eq. (2.35). A computationally more efficient approach is the absorber doubling method [41, 75], which proceeds as follows. Consider a step x that is small compared to the mean free path such that $\langle n \rangle \ll 1$ (in practice: $\langle n \rangle < 0.01$ [76]). Expanding Eq. (2.35) in powers of $\langle n \rangle$ and retaining only constant and linear terms gives

$$f(E, x) \sim (1 - \langle n \rangle) f^{(0)}(E) + \langle n \rangle f^{(1)}(E) .$$

The straggling function for a distance $2x$ is then calculated using

$$f(\Delta, 2x) = \int_0^{\Delta} f(\Delta - E, x) f(E, x) \, \mathrm{d}E .$$

This procedure is carried out k times until the desired thickness $2^k x$ is reached. Because of the tail of $f^{(1)}(E)$ towards large energy transfers, the numerical convolution is performed on a logarithmic grid. More details of the implementation can be found in Refs. [75, 76].

2.5.3 Laplace Transforms

In the Laplace domain, Eq. (2.35) becomes

$$F(s,x) = \mathcal{L}\{f(\Delta,x)\} = \mathrm{e}^{-\langle n\rangle}\sum_{n=0}^{\infty}\frac{\langle n\rangle^n}{n!}\mathcal{L}\{f^{(1)}(\Delta)\}^n$$
$$= \exp\left[-Nx\int_0^{\infty}\mathrm{d}E\left(1-\mathrm{e}^{-sE}\right)\frac{\mathrm{d}\sigma}{\mathrm{d}E}\right].$$

Following Landau [20], we split the integral in the exponent in two parts,

$$Nx\int_0^{\infty}\mathrm{d}E\left(1-\mathrm{e}^{-sE}\right)\frac{\mathrm{d}\sigma}{\mathrm{d}E} = Nx\int_0^{E_1}\mathrm{d}E\left(1-\mathrm{e}^{-sE}\right)\frac{\mathrm{d}\sigma}{\mathrm{d}E} + Nx\int_{E_1}^{\infty}\mathrm{d}E\left(1-\mathrm{e}^{-sE}\right)\frac{\mathrm{d}\sigma}{\mathrm{d}E},$$

where E_1 is chosen to be large compared to the ionisation threshold while at the same time satisfying $sE_1 \ll 1$. For energy transfers exceeding E_1, the differential cross section is assumed to be given by the asymptotic expression for close collisions (2.11); for $E < E_1$, it is not specified.

Using $\exp(-sE) \sim 1 - sE$, we obtain for the first term

$$I_1 = Nx\int_0^{E_1}\mathrm{d}E\frac{\mathrm{d}\sigma}{\mathrm{d}E}\left(1-\mathrm{e}^{-sE}\right) \sim Nxs\int_0^{E_1}\mathrm{d}E\frac{\mathrm{d}\sigma}{\mathrm{d}E}E.$$

We can therefore evaluate I_1 by subtracting the contribution due to energy transfers between E_1 and $E_{\max}$ according to Eq. (2.11) from the total average energy loss $x\mathrm{d}E/\mathrm{d}x = \langle\Delta\rangle$,

$$I_1 \sim s\langle\Delta\rangle - s\xi\left(\ln\frac{E_{\max}}{E_1} - \beta^2\right),$$

where we have introduced the variable

$$\xi = x\frac{2\pi z^2(\alpha\hbar c)^2 NZ}{mc^2\beta^2}.$$

For evaluating the second integral, we approximate $\mathrm{d}\sigma/\mathrm{d}E$ by the Rutherford cross section $\mathrm{d}\sigma_R/\mathrm{d}E \propto 1/E^2$. Because of the rapid convergence of the integral for $sE \gg 1$, we further assume that the upper integration limit can be extended to infinity (instead of truncating $\mathrm{d}\sigma/\mathrm{d}E$ at $E_{\max}$). Integrating by parts and substituting $z = sE$ yields

$$I_2 = \xi \int_{E_1}^{\infty} \mathrm{d}E \frac{1-\mathrm{e}^{-sE}}{E^2} = \xi \underbrace{\frac{1-\mathrm{e}^{-sE_1}}{E_1}}_{\sim s} + \xi s \int_{sE_1}^{\infty} \mathrm{d}z \frac{\mathrm{e}^{-z}}{z} \sim \xi s \left(1 + \int_{sE_1}^{1} \frac{\mathrm{d}z}{z} - C\right),$$

where $C \sim 0.577215665$ is Euler's constant.[3] Combining the two terms I_1 and I_2, one obtains

$$F(s,x) = \exp\left[-\xi s \left(1 - C + \frac{\langle\Delta\rangle}{\xi} - \ln sE_{\max} + \beta^2\right)\right],$$

and, applying the inverse Laplace transform,

$$f(\Delta, x) = \mathcal{L}^{-1}\{F(s,x)\} = \frac{1}{\xi}\phi_L(\lambda), \tag{2.37}$$

where

$$\phi_L(\lambda) = \frac{1}{2\pi\mathrm{i}} \int_{c-\mathrm{i}\infty}^{c+\mathrm{i}\infty} \mathrm{d}u\, \mathrm{e}^{u\ln u + \lambda u}. \tag{2.38}$$

is a universal function of the dimensionless variable

$$\lambda = \frac{\Delta - \langle\Delta\rangle}{\xi} - (1-C) - \beta^2 - \ln\frac{\xi}{E_{\max}}.$$

The maximum of $\phi_L(\lambda)$ is located at $\lambda \sim -0.222782$ and the most probable energy loss is, consequently, given by

$$\Delta_{\mathrm{p}} \sim \langle\Delta\rangle + \xi\left(0.2 + \beta^2 + \ln\kappa\right), \tag{2.39}$$

[3] $$-C = \int_0^1 \mathrm{d}z \frac{\mathrm{e}^{-z}-1}{z} + \int_1^{\infty} \mathrm{d}z \frac{\mathrm{e}^{-z}}{z} = -0.577215665\ldots$$

where $\kappa = \xi/E_{\max}$. The full width at half maximum (FWHM) of the Landau distribution[4] (2.37) is approximately 4.02ξ.

A somewhat unsatisfactory aspect of $\phi_L(\lambda)$ is that its mean is undefined (a consequence of allowing arbitrarily large energy transfers $E > E_{\max}$). This deficiency was overcome by Vavilov [77] who, taking account of the kinematically allowed maximum energy transfer $E_{\max}$ and using the differential cross section (2.11) in I_2, obtained

$$f(\Delta, x) = \frac{1}{\xi}\phi_V(\lambda), \qquad \phi_V(\lambda) = \frac{1}{2\pi \mathrm{i}} \mathrm{e}^{\kappa\left(1+\beta^2 C\right)} \int_{c-\mathrm{i}\infty}^{c+\mathrm{i}\infty} \exp\left(\psi(u) + \lambda u\right) \mathrm{d}u,$$

where

$$\psi(u) = u \ln \kappa + \left(u + \beta^2 \kappa\right) \left(\int_{u/\kappa}^{\infty} \frac{\mathrm{e}^{-t}}{t} \mathrm{d}t + \ln \frac{u}{\kappa} \right) - \kappa \mathrm{e}^{-u/\kappa}.$$

For small values of κ ($\kappa < 0.01$ [77]) the Vavilov distribution tends to the Landau distribution, while for $\kappa \gg 1$ it approaches a Gaussian distribution with $\sigma^2 = \xi E_{\max}\left(1 - \beta^2/2\right)$ [78]. Algorithms for the numerical evaluation of ϕ_L and ϕ_V and for drawing random numbers from these distributions are discussed e.g. in Refs. [78–81] and are implemented in ROOT [82].

Attempts have been made [83, 84] to improve the Landau-Vavilov method with respect to the treatment of distant collisions by including the second order term in the expansion of $\exp(-sE)$ in I_1. The results are akin to convolving ϕ_L or ϕ_V with a Gaussian distribution (expressions for estimating the standard deviation σ of the Gaussian are reviewed in Ref. [41]).

2.5.4 Examples

Let us first consider track segments for which the projectile suffers on average only tens of collisions. At the minimum of M_0, $\langle n \rangle = 10$ corresponds to a track length $x \sim 4\,\mathrm{mm}$ for argon (at atmospheric pressure, $T = 20\,^{\circ}\mathrm{C}$) and $x \sim 2\,\mu\mathrm{m}$ for silicon (Tables 2.1 and 2.2). As can be seen from Figs. 2.11 and 2.12, the features of the differential cross section $\mathrm{d}\sigma/\mathrm{d}E$ are clearly visible in the straggling functions $f(\Delta, x)$. These spectra cannot be described by a Landau distribution (or variants thereof) and need to be calculated using Monte Carlo simulation or numerical convolution.

[4] In high-energy physics parlance, the term "Landau distribution" is sometimes used for energy loss spectra $f(\Delta, x)$ in general. In this chapter, it refers only to the distribution given by Eq. (2.37).

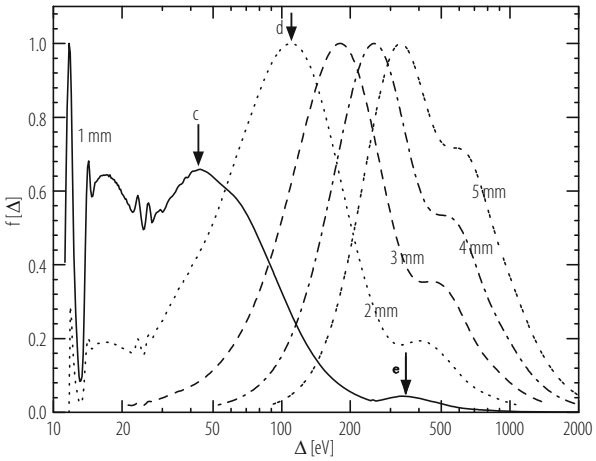

Fig. 2.11 Straggling functions for singly charged particles with $\beta\gamma = 4.48$ traversing segments of length $x = 1 \ldots 5$ mm in Ar. The inverse mean free path M_0 is 30 collisions/cm. The functions are normalised to unity at the most probable value. The broad peak at ∼17 eV is due to single collisions, see Fig. 2.9. For two collisions it broadens and shifts to about 43 eV, marked c, and for $n = 3$ it can be seen at d. It may be noted that the peak at 11.7 eV (if the function is normalised to unit area) is exactly proportional to $\langle n \rangle \exp(-\langle n \rangle)$, as expected from Eq. (2.35). Energy losses to L-shell electrons of Ar (with a binding energy of ∼250 eV) appear at e, for $x = 1$ mm they have an amplitude of 0.04. For $x > 2$ mm, peak c disappears, and peak d becomes the dominant contribution defining the most probable energy loss Δ_p. The buildup for peak e at 440–640 eV is the contribution from L-shell collisions. It appears roughly at 250 eV+Δ_p. The inverse mean free path for collisions with $E > 250$ eV is only 1.7 collisions/cm, thus the amplitude of the peak e is roughly proportional to x. The Bethe mean energy loss is 250 eV/mm

With increasing number of collisions, the detailed features of the differential cross section become "washed out" and the energy loss spectra $f(\Delta, x)$ tend to the Landau shape but are typically broader, as shown in Figs. 2.13 and 2.14. Reasonable agreement with measured energy loss spectra for thin absorbers can often be achieved by fit functions based on the convolution of a Landau/Vavilov distribution and a Gaussian distribution. For a predictive calculation of $f(\Delta, x)$, however, numerical convolution or a Monte Carlo simulation are usually needed.

2.5.5 *Methods for Thick Absorbers*

In order to compute the energy loss distribution for a layer of material in which the kinetic energies T of the traversing particles change considerably (i.e. by more than 5–10% [86]), we divide the absorber in segments of length x that are sufficiently small such that the straggling function $f(\Delta, x)$ can be calculated using the methods for thin absorbers described above. Let $\phi(y, T)$ be the distribution of

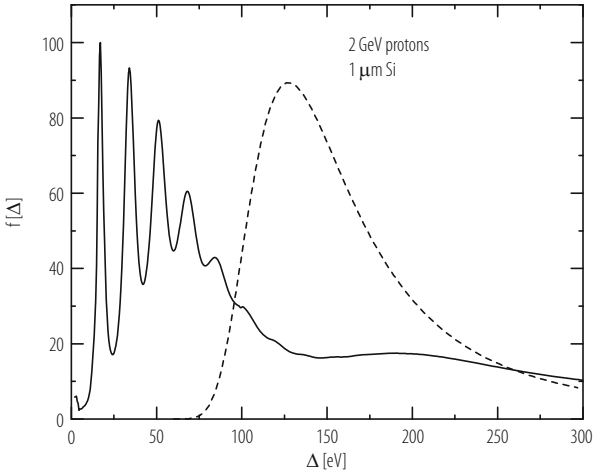

Fig. 2.12 Straggling in 1 μm of Si ($\langle n \rangle = 4$) for particles with $\beta\gamma = 2.1$, compared to the Landau function (dashed line). The Bethe mean energy loss is $\langle \Delta \rangle = 400$ eV. Measured straggling functions of this type are given in Ref. [85]

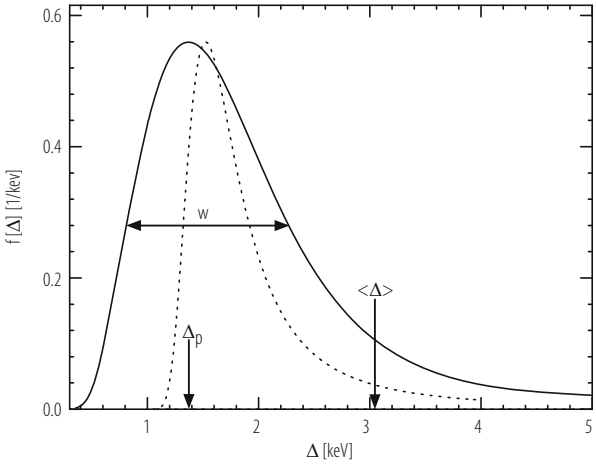

Fig. 2.13 Straggling function $f(\Delta)$ for particles with $\beta\gamma = 3.6$ traversing 1.2 cm of Ar gas ($\langle n \rangle = 36$) calculated using the convolution method (solid line) compared to the Landau distribution (dashed line). Parameters describing $f(\Delta)$ are the most probable energy loss Δ_p, i.e. the position of the maximum of the straggling function, at 1371 eV, and the full width at half maximum (FWHM) $w = 1463$ eV. The Bethe mean energy loss is $\langle \Delta \rangle = 3044$ eV. The peak of the Landau function is at 1530 eV

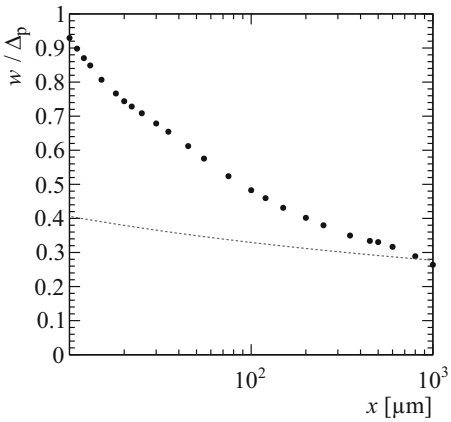

Fig. 2.14 Relative width (full width at half maximum w divided by the most probable value Δ_p) of the straggling spectrum $f(\Delta, x)$ as function of the absorber thickness x, for particles with $\beta\gamma \sim 3.16$ in silicon. The dashed line corresponds to the relative width of the Landau distribution. Circles represent results of a Monte Carlo simulation using the Bethe-Fano differential cross section

kinetic energies at a distance y in the absorber. If $f(\Delta, x)$ is known for all T, the spectrum of kinetic energies at $y + x$ can be calculated using

$$\phi(y + x, T) = \int \phi(y, T + \Delta)\, f(\Delta, x; T + \Delta)\, \mathrm{d}\Delta.$$

Scaling relations, discussed in Ref. [51], can be used to limit the number of thin-absorber distributions $f(\Delta, x; T)$ that need to be tabulated.

In a "condensed history" Monte Carlo simulation [87], the energy loss spectrum is calculated stochastically by sampling the energy loss over a substep x from a suitable thin-absorber distribution (e.g. a Vavilov function), and updating the kinetic energy T of the projectile after each substep.

2.6 Energy Deposition

Leaving the emission of Cherenkov radiation and other collective effects aside, charged-particle collisions with electrons in matter result in the promotion of one of the electrons in the target medium to a bound excited state or to the continuum. Both effects (excitation and ionisation) can be exploited for particle detection purposes. In scintillators, discussed in Chap. 3 of this book, part of the energy transferred to excitations is converted to light. Detectors based on ionisation measurement in gases and semiconductors are discussed in Chaps. 4 and 5. In the following we briefly review the main mechanisms determining the number of electron-ion pairs (in gases) or electron-hole pairs (in semiconductors) produced in the course of an ionising collision, along with their spatial distribution.

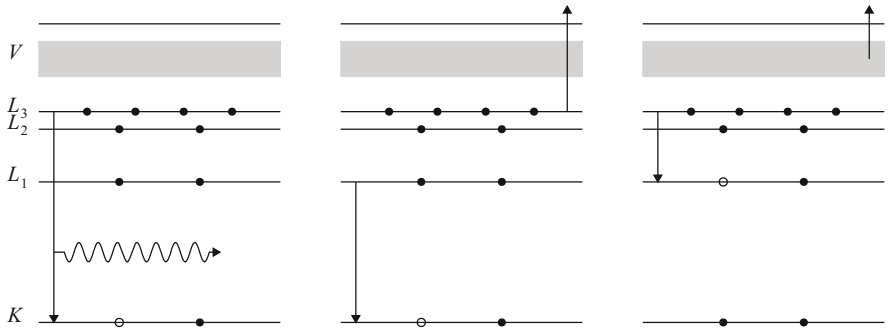

Fig. 2.15 After the ejection of an inner-shell electron, the resulting vacancy is filled by an electron from a higher shell. The energy released in the transition can either be carried away by a fluorescence photon (left) or be transferred to an electron in a higher shell (Auger process, middle). Coster-Kronig transitions (right) are Auger processes in which the initial vacancy is filled by an electron from the same shell

2.6.1 Atomic Relaxation

If a charged-particle collision (or a photoabsorption interaction) ejects an inner-shell electron from an atom, the resulting vacancy will subsequently be filled by an electron from a higher shell, giving rise to a relaxation chain which can proceed either radiatively, i.e. by emission of a fluorescence photon, or radiation-less (Auger effect). The two processes are illustrated schematically in Fig. 2.15. Fluorescence photons can in turn ionise another atom in the medium or, with a probability depending on the geometry of the device, escape from the detector. The fluorescence yield, i.e. the probability for a vacancy to be filled radiatively, increases with the atomic number Z: in silicon, for example, the average fluorescence yield is $\sim$5%, compared to $\sim$54% in germanium [88]. Compilations of fluorescence yields can be found in Refs. [88–91]. Tabulations of transition probabilities are available in the EADL database [92, 93].

2.6.2 Ionisation Statistics

The "primary" ionisation electron knocked out in a collision (and also the Auger electrons) may have kinetic energies exceeding the ionisation threshold of the medium and thus undergo further ionising collisions along their path. Electrons with a kinetic energy T that is large compared to the ionisation threshold are referred to as "delta" electrons; their energy distribution follows approximately the close-collision differential cross section, given by Eq. (2.11) for spin-zero particles. The number of electrons n_e produced in the energy degradation cascade of a delta electron with initial kinetic energy T is subject to fluctuations. The mean and variance of the

distribution of n_e are described by the average energy W required to produce an electron-ion (electron-hole) pair,

$$\langle n_e \rangle = \frac{T}{W}, \tag{2.40}$$

and the Fano factor F [94],

$$\sigma^2 = \langle (n - \langle n \rangle)^2 \rangle = F \langle n_e \rangle, \tag{2.41}$$

respectively. Both W and F are largely determined by the relative importance of ionising and non-ionising inelastic collisions, the latter including e.g. excitations or phonon scattering. If the cross sections for these processes are known, the distribution of n_e can be calculated using detailed Monte Carlo simulations. An example is the MAGBOLTZ program [95, 96], which includes the relevant cross sections for many commonly used detection gases. Inelastic cross sections of delta electrons in solids can be calculated based on the dielectric formalism discussed in Sect. 2.3.1 (in its non-relativistic version), often making using of optical data and a suitable model of the q-dependence of $\mathrm{Im}\,(-1/\varepsilon\,(q, E))$ as, for instance, in the Penn algorithm described in Ref. [97].

Measurements of W for electrons in gases as a function of the electron's initial kinetic energy are reported in Refs. [98–100, 102, 103]. As can be seen from Fig. 2.16, which shows measurements and calculations for CO_2, W increases towards low kinetic energies, while in the keV range and above it depends only weakly on T. For most gases and semiconductors typically used as sensitive media in particle detectors, the asymptotic (high-energy) W values are fairly well established. A compilation of recommended average W values, based on experimental data until 1978, is given in ICRU report 31 [101]. Critical reviews of W values and Fano factors including also more recent data can be found in Ref. [104]

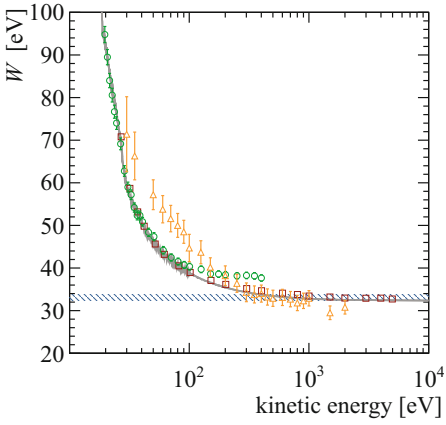

Fig. 2.16 W value for electrons in CO_2 as a function of the electron's initial kinetic energy according to measurements by Combecher [98] (circles), Smith and Booz [99] (triangles), and Waibel and Grosswendt [100] (squares). The grey band represents results of a Monte Carlo calculation using the cross sections implemented in MAGBOLTZ [96]. The hatched band corresponds to the high-energy value recommended in Ref. [101]

Table 2.3 Asymptotic W values and Fano factors for different gases and for solid silicon (at $T = 300\,\mathrm{K}$)

	W [eV]	F
Ne	35.4 ± 0.9 [101]	0.13–0.17 [104]
Ar	26.4 ± 0.5 [101]	0.15–0.17 [104]
Kr	24.4 ± 0.3 [101]	0.17–0.21 [104]
Xe	22.1 ± 0.1 [101]	0.124–0.24 [104]
CO_2	33.0 ± 0.7 [101]	0.32 [104]
CH_4	27.3 ± 0.3 [101]	0.22–0.26 [104]
iC_4H_{10}	23.4 ± 0.4 [101]	0.261 [106]
CF_4	34.3 [107]	
Si	3.67 ± 0.02 [108]	<0.1 [104]

Except for CF_4, the values shown are for measurements using electrons

and, with emphasis on noble gases, in Ref. [105]. Parameters for silicon and some commonly used gases are listed in Table 2.3.

Analogously to Eqs. (2.40) and (2.41) one can define W values and Fano factors characterising the distribution of the number of electrons produced by a heavy charged particle (provided that it is stopped completely in the medium) or by the absorption of a photon. The asymptotic W values for electrons and photons at high energies are in general very similar.

In gas mixtures without excitation transfers, the W value and Fano factor are, to a good approximation, given by the values in the pure gases, weighted by their respective concentrations. In mixtures where one of the components has excited states with energies exceeding the ionisation threshold of another component, excitation transfer can lead to a significant reduction of W and F with respect to the pure gases ("Jesse effect" [109]). Results for a number of binary gas mixtures from measurements with α particles can be found in Ref. [110].

2.6.3 Range

The spatial distribution of secondary ionisations produced by a delta electron can be characterised in terms of the electron range, i.e. the typical path length travelled by an electron before its energy falls below the ionisation threshold. In the literature, a number of different definitions of "range" exist, two of which—the fractional ionisation range R_x and the practical range R_p—are illustrated in Fig. 2.17. If the cross sections (including those for elastic scattering) are known, the range of delta electrons and, more generally, the ionisation pattern produced by a charged-particle collision, can be calculated using Monte Carlo techniques. As an example, Fig. 2.18 shows measurements of the 95% range in CH_4 as a function of the primary electron energy [102], together with calculated values based on the cross sections implemented in MAGBOLTZ.

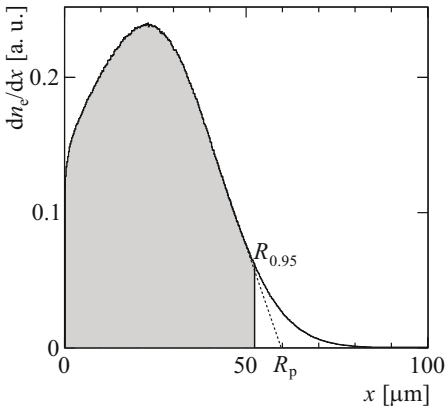

Fig. 2.17 Distribution of the coordinates (projected on the electron's initial direction) of ionising collisions by a $T = 1$ keV electron and its secondaries in methane (at atmospheric pressure, $T = 20\,°C$), calculated using the cross sections implemented in MAGBOLTZ. The fractional ionisation range R_x is defined as the projected distance along the electron's initial direction within which the fraction x of the total ionisation is produced [102]. The practical range R_p is determined by linear extrapolation from the region of steepest descent to the horizontal axis

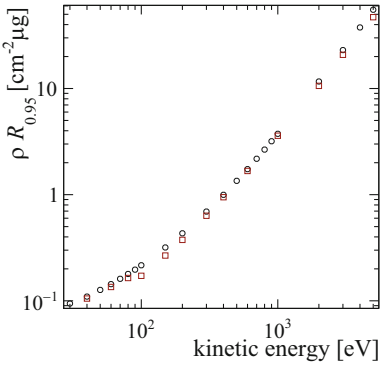

Fig. 2.18 Measurements [102] (squares) and MAGBOLTZ calculations (circles) of the 95% fractional ionisation range of electrons in methane (at atmospheric pressure)

In the absence of a detailed calculation, the semi-empirical formula by Kobetich and Katz [111, 112] can be used to estimate the practical range,

$$\rho R_p\,(T) = AT\left(1 - \frac{B}{1 + CT}\right),$$

where the parameters A, B, C are given by [112]

$$A = \left(0.81Z^{-0.38} + 0.18\right) \times 10^{-3}\,\mathrm{g\,cm^{-2}\,keV^{-1}},$$
$$B = 0.21Z^{-0.055} + 0.78,$$
$$C = \left(1.1Z^{0.29} + 0.21\right) \times 10^{-3}\,\mathrm{keV^{-1}}.$$

References

1. U. Fano, Annu. Rev. Nucl. Sci. **13**, 1 (1963).
2. M. Inokuti, Rev. Mod. Phys. **43**, 297 (1971).
3. M. Inokuti, Rev. Mod. Phys. **50**, 23 (1978).
4. H. Bichsel, Passage of Charged Particles Through Matter, in *Amer. Instrum. Phys. Handbook*, edited by D. E. Gray, McGraw Hill, 1972.
5. R. J. Gould, Physica **62**, 555 (1972).
6. W. W. M. Allison and J. H. Cobb, Annu. Rev. Nucl. Part. Sci. **30**, 253 (1980).
7. S. P. Ahlen, Rev. Mod. Phys. **52**, 121 (1980).
8. B. Rossi, *High-Energy Particles*, Prentice-Hall, New York, NY, 1952.
9. R. D. Evans, *The Atomic Nucleus*, McGraw Hill, 1967.
10. W. Heitler, *The Quantum Theory of Radiation, second edition*, Oxford University Press, 1949.
11. P. Sigmund, *Particle Penetration and Radiation Effects*, Springer, 2006.
12. N. J. Carron, *An Introduction to the Passage of Energetic Particles through Matter*, Taylor and Francis, 2007.
13. B. McParland, *Medical radiation dosimetry: Theory of charged particle collision energy loss*, Springer, 2014.
14. N. Bohr, Philos. Mag. **25**, 10 (1913).
15. N. Bohr, Philos. Mag. **30**, 581 (1915).
16. H. Bethe, Ann. Phys. **5**, 325 (1930).
17. H. Bethe, Z. Phys. **76**, 293 (1932).
18. E. Fermi, Z. Phys. **29**, 3157 (1924).
19. E. Fermi, Phys. Rev. **57**, 485 (1940).
20. L. D. Landau, J. Phys. USSR **8**, 201 (1944).
21. U. Fano, L. V. Spencer, and M. J. Berger, Penetration and Diffusion of X Rays, in *Handbuch der Physik*, edited by S. Flügge, volume 38/2, Springer, 1959.
22. W. Rösch, E. Tochilin, and F. H. Attix, editors, *Radiation Dosimetry; 2nd ed.*, Academic Press, 1968.
23. F. Salvat and J. M. Fernandez-Varea, Metrologia **46**, S112 (2009).
24. M. J. Berger et al., XCOM: Photon Cross Sections Database, https://www.nist.gov/pml/xcom-photon-cross-sections-database.
25. J. Berkowitz, *Atomic and molecular photo absorption*, Academic Press, 2002.
26. N. Sakamoto et al., Oscillator Strength Spectra and Related Quantities of 9 Atoms and 23 Molecules Over the Entire Energy Region, NIFS-DATA-109, National Institute for Fusion Science, 2010, available online at http://www.nifs.ac.jp/report/nifsdata.html.
27. B. L. Henke, E. M. Gullikson, and J. C. Davis, Atomic Data and Nucl. Data Tables **54**, 181 (1993), available online at http://henke.lbl.gov/optical_constants/.
28. J.-J. Yeh and I. Lindau, Atomic Data and Nucl. Data Tables **32**, 1 (1985).

29. M. B. Trzhaskovskaya, V. I. Nefedov, and V. G. Yarzhemsky, Atomic Data and Nucl. Data Tables **77**, 97 (2001).
30. M. B. Trzhaskovskaya, V. I. Nefedov, and V. G. Yarzhemsky, Atomic Data and Nucl. Data Tables **82**, 257 (2002).
31. E. D. Palik and E. J. Prucha, *Handbook of optical constants of solids*, Academic Press, 1998.
32. S. Adachi, *Optical constants of crystalline and amorphous semiconductors*, Kluwer Academic Publishers, 1999.
33. O. Klein and Y. Nishina, Z. Physik **52**, 853 (1929).
34. J. H. Hubbell, Photon Cross Sections, Attenuation Coefficients, and Energy Absorption Coefficients from 10 keV to 100 GeV, NSRDS-NBS 29, National Bureau of Standards, 1969, available online at https://www.nist.gov/srd/national-standard-reference-data-series.
35. P. M. Bergstrom and R. H. Pratt, Radiation Physics and Chemistry **50**, 3 (1997).
36. J. H. Hubbell, H. A. Gimm, and I. Øverbø, J. Phys. Chem. Ref. Data **9**, 1023 (1980).
37. D. Bote and F. Salvat, Phys. Rev. A **77**, 042701 (2008).
38. L. D. Landau, E. M. Lifshitz, and L. P. Pitaevskii, *Electrodynamics of Continuous Media*, Butterworth, 1984.
39. J. Lindhard, Mat. Fys. Medd. Dan. Vid. Selsk. **28**, 1 (1954).
40. J. Lindhard and A. Winther, Mat. Fys. Medd. Dan. Vid. Selsk. **34**, 1 (1964).
41. H. Bichsel, Rev. Mod. Phys. **60**, 663 (1988).
42. H. Bichsel, Phys. Rev. A **65**, 052709 (2002).
43. H. Bichsel, Phys. Rev. A **46**, 5761 (1992).
44. H. Bichsel, K. M. Hanson, and M. E. Schillaci, Phys. Med. Biol. **27**, 959 (1982).
45. M. C. Walske, Phys. Rev. **88**, 1283 (1952).
46. M. C. Walske, Phys. Rev. **101**, 1940 (1956).
47. V. A. Chechin, L. P. Kotenko, G. I. Merson, and V. C. Yermilova, Nucl. Instr. Meth. **98**, 577 (1972).
48. F. Lapique and F. Piuz, Nucl. Instr. Meth. **175**, 297 (1980).
49. I. B. Smirnov, Nucl. Instr. Meth. A **554**, 474 (2005).
50. J. Apostolakis et al., Nucl. Instr. Meth. A **453**, 597 (2000).
51. H. Bichsel, Nucl. Instrum. Meth. A **562**, 154 (2006).
52. F. Rieke and W. Prepejchal, Phys. Rev. A **6**, 1507 (1972).
53. R. P. Saxon, Phys. Rev. A **8**, 839 (1973).
54. M. Inokuti, R. P. Saxon, and J. L. Dehmer, Int. J. Radiat. Phys. Chem. **7**, 109 (1975).
55. B. Sitar, G. I. Merson, V. A. Chechin, and Y. A. Budagov, *Ionization Measurements in High Energy Physics*, Springer, 1993.
56. G. W. McClure, Phys. Rev. **90**, 796 (1953).
57. G. Malamud, A. Breskin, R. Chechik, and A. Pansky, J. Appl. Phys. **74**, 3645 (1993).
58. H. A. Bethe and R. W. Jackiw, *Intermediate quantum mechanics*, Benjamin, 1986.
59. R. M. Sternheimer, M. J. Berger, and S. M. Seltzer, Atomic Data and Nucl. Data Tables **30**, 261 (1984).
60. *Stopping powers and ranges for protons and alpha particles*, International Commission on Radiation Units and Measurements, Washington, DC, 1993, ICRU Report 49.
61. M. J. Berger, J. S. Coursey, M. A. Zucker, and J. Chang, ESTAR, PSTAR, and ASTAR: Computer Programs for Calculating Stopping-Power and Range Tables for Electrons, Protons, and Helium Ions, http://physics.nist.gov/Star.
62. D. E. Groom, N. V. Mokhov, and S. I. Striganoff, Atomic Data and Nucl. Data Tables **78**, 183 (2001).
63. W. H. Barkas, J. N. Dyer, and H. H. Heckman, Phys. Rev. Lett. **11**, 26 (1963).
64. H. H. Andersen, H. Simonsen, and H. Sørensen, Nuclear Physics A **125**, 171 (1969).
65. H. Bichsel, Phys. Rev. A **41**, 3642 (1990).
66. E. A. Uehling, Annu. Rev. Nucl. Sci. **4**, 315 (1954).
67. *Stopping powers for electrons and positrons*, International Commission on Radiation Units and Measurements, Washington, DC, 1979, ICRU Report 37.
68. H. Bethe and W. Heitler, Proc. Roy. Soc. A **146**, 83 (1934).

69. H. W. Koch and J. W. Motz, Rev. Mod. Phys. **31**, 920 (1959).
70. M. Tanabashi et al., Phys. Rev. D **98**, 030001 (2018).
71. D. E. Groom, Atomic and Nuclear Properties of Materials, http://pdg.lbl.gov/AtomicNuclearProperties.
72. E. J. Williams, Proc. Roy. Soc. A **125**, 420 (1929).
73. H. Bichsel and R. P. Saxon, Phys. Rev. A **11**, 1286 (1975).
74. F. Salvat, J. M. Fernández-Varea, and J. Sempau, PENELOPE-2014: A Code System for Monte Carlo Simulation of Electron and Photon Transport.
75. A. M. Kellerer, *Mikrodosimetrie*, Strahlenbiologisches Institut der Universität München, 1968, G.S.F. Bericht B-1.
76. A. M. Kellerer, Fundamentals of Microdosimetry, in *The Dosimetry of Ionizing Radiation*, edited by K. R. Kase, B. E. Bjängard, and F. H. Attix, Academic Press, 1985.
77. P. V. Vavilov, Sov. Phys. JETP **5**, 749 (1957).
78. M. J. Berger and S. M. Seltzer, *Studies in Penetration of Charged Particles in Matter*, The National Academies Press, Washington, DC, 1964.
79. W. Boersch-Supan, J. Res. Nat. Bur. Stand. **65B**, 245 (1961).
80. B. Schorr, Computer Phys. Comm. **7**, 215 (1974).
81. A. Rotondi and P. Montagna, Nucl. Instr. Meth. B **47**, 215 (1990).
82. R. Brun et al., Nucl. Instrum. Meth. A **389**, 81 (1997), http://root.cern.ch.
83. O. Blunck and S. Leisegang, Z. Phys. **128**, 500 (1950).
84. P. Shulek et al., Sov. J. Nucl. Phys. **4**, 400 (1967).
85. J. P. Perez, J. Sevely, and B. Jouffrey, Phys. Rev. A **16**, 1061 (1977).
86. C. Tschalär, Nucl. Instrum. Meth. **61**, 141 (1968).
87. M. J. Berger, Meth. Comput. Phys. **1**, 135 (1963).
88. M. O. Krause, J. Phys. Chem. Ref. Data **8**, 307 (1979).
89. W. Bambynek et al., Rev. Mod. Phys. **44**, 716 (1972).
90. J. H. Hubbell et al., J. Phys. Chem. Ref. Data **23**, 339 (1994).
91. J. H. Hubbell et al., J. Phys. Chem. Ref. Data **33**, 621 (2004).
92. S. T. Perkins et al., Tables and Graphs of Atomic Subshell and Relaxation Data Derived from the LLNL Evaluated Atomic Data Library (EADL), $Z = 1 - 100$, UCRL-50400, Lawrence Livermore National Laboratory, Livermore, CA, 1991.
93. D. E. Cullen, EPICS2017. Electron and Photon Interaction Cross Sections, https://www-nds.iaea.org/epics/.
94. U. Fano, Phys. Rev. **72**, 26 (1947).
95. S. F. Biagi, Nucl. Instr. Meth. A **421**, 234 (1999).
96. S. F. Biagi, Magboltz 8, http://magboltz.web.cern.ch/magboltz.
97. D. R. Penn, Phys. Rev. B **35**, 482 (1987).
98. D. Combecher, Radiation Research **84**, 189 (1980).
99. B. G. R. Smith and J. Booz, Experimental results on W-values and transmission of low energy electrons in gases, in *Sixth Symposium on Microdosimetry*, page 759, 1978.
100. E. Waibel and B. Grosswendt, Nucl. Instr. Meth. B **53**, 239 (1991).
101. *Average energy required to produce an ion pair*, International Commission on Radiation Units and Measurements, Washington, DC, 1979, ICRU Report 31.
102. E. Waibel and B. Grosswendt, Nucl. Instr. Meth. **211**, 487 (1983).
103. E. Waibel and B. Grosswendt, Study of W-values, practical ranges, and energy dissipation profiles of low-energy electrons in N_2, in *Eighth Symposium on Microdosimetry*, page 301, 1983.
104. Atomic and Molecular Data for Radiotherapy and Radiation Research, IAEA TECDOC 799, 1995.
105. I. Krajcar Bronić, Hoshasen: ionizing radiation **24**, 101 (1998).
106. D. Srdoč, B. Obelić, and I. Krajcar Bronić, J. Phys. B: At. Mol. Phys. **20**, 4473 (1987).
107. G. F. Reinking, L. G. Christophorou, and S. R. Hunter, J. Appl. Phys. **60**, 499 (1986).
108. R. H. Pehl, F. S. Goulding, D. A. Landis, and M. Lenzlinger, Nucl. Instr. Meth. **59**, 45 (1968).
109. W. P. Jesse and J. Sadauskis, Phys. Rev. **88**, 417 (1952).

110. T. E. Bortner, G. S. Hurst, M. Edmundson, and J. E. Parks, Alpha particle ionization of argon mixtures – further study of the role of excited states, ORNL-3422, Oak Ridge National Laboratory, 1963.
111. E. J. Kobetich and R. Katz, Phys. Rev. **170**, 391 (1968).
112. E. J. Kobetich and R. Katz, Nucl. Instr. Meth. **71**, 226 (1969).